Periodic precipitation and coarsening waves: Applications of the competitive particle growth model[a)]

R. Feeney,[b)] S. L. Schmidt,[b)c)] P. Strickholm,[b)] J. Chadam,[d)] and P. Ortoleva[b)e)f)]

Indiana University, Bloomington, Indiana 47405
(Received 24 August 1981; accepted 4 March 1982)

It has been shown earlier that the competitive growth dynamics of particles in a sol can account for spontaneous precipitation patterns that arise as a uniform sol ages. Here it is found that this dynamics can, unlike the classic Ostwald–Prager theory, account for a complete range of precipitation pattern types including Runge–Liesegang bands, invert bands, secondary banding, spontaneous pattern formation from a uniform sol and propagation, and destabilization of fronts of coarsening. Effects of electrical fields on banding are also investigated. A characteristic length is obtained and is found to be a strictly nonlinear effect.

I. INTRODUCTION

Interest in spatially periodic precipitation has spanned the last century. Studies of regular precipitation bands seem to have originated with Runge and later with Liesegang,[1] the phenomenon having been named after the latter. The early work is reviewed in the 1926 book by Hedges and Myers entitled *Physico–Chemical Periodicity*.[2] These authors also conjectured that the mechanism of a number of geological and biological patterning phenomena could be essentially the same as precipitation banding (see also Ref. 3). The more modern literature is surveyed in Ref. 4.

The classic theory of this phenomenon was set forth by Ostwald[5] and Prager.[6] In their model, interdiffusing coprecipitates supersaturate in some interface zone. This is followed by nucleation and ensuing depletion of soluble coprecipitate species until one of them diffuses further into the domain rich in the other, commencing a new sequence of supersaturation and nucleation. This theory relies strongly on the cross diffusion configuration and cannot explain either the origin of secondary banding (one band breaking up into a sequence of more closely spaced bands), or invert spacing (the spacing between the bands is usually observed to increase down a tube of gel solution of one of the coprecipitates over which the other reactant is superimposed).

Another theory of the bands involves a mechanism of autocatalytic creation of precipitate particles.[7] Although there does not seem to be any physical justification of such a mechanism, it does lead to an interesting pattern forming dynamics.

A more recent theoretical approach is based on a feedback involving particle growth, diffusion, and the precipitate particle size dependence of the equilibrium concentration due to surface tension.[8,9] This mechanism leads to coarsening of a sol.[10] In Sec. II, we shall review this model. In the remainder of this paper, we show that this theory can explain a host of spatio–temporal precipitation phenomena, including a number of phenomena that are contradictory to the Ostwald–Prager theory. These effects have also been observed experimentally; some of these results are also presented although a more complete account of the experiments and comparison with theory is given elsewhere.[13] We conclude by pointing out that the mathematical structure of the present problem is a exemplary case of a wide class of spontaneous pattern formation phenomena involving the coupling of transport and first order phase transitions.[3,18,19]

II. COMPETITIVE PARTICLE GROWTH THEORY

A. Phase transition kinetics

The kinetics of band formation is that of a first order phase transition coupled to transport. A chemical kinetic model of precipitation kinetics is the sequence of binary processes

$$P_m + P_n \rightleftarrows P_{m+n}\,, \tag{II. A1}$$

where $P_n, n = 1, 2, \ldots$ is an aggregate of n moments. A more modest description of the particle growth/dissolution process is to limit Eq. (II. A1) to monomer addition

$$P_n + P_1 \rightleftarrows P_{n+1}\,. \tag{II. A2}$$

This picture is applicable when precipitate particle density is low and stirring is absent. A fuller discussion of these models and their ranges of vailidity is found in Ref. 11. We shall adopt a simplified version of model (II. A2) here.

For model (II. A2), a description of the system is in terms of the concentrations $\mathbf{c} = \{c_1, c_2, \ldots, c_n, \ldots\} = \mathbf{c}(\mathbf{r}, t)$ at all points $\mathbf{r}$ and times t. In Ref. 9, such a description of spontaneous pattern formation was set forth. It is our purpose here to study a simpler description that is strictly valid after nucleation and when c_n is narrowly peaked about some $n^*(\mathbf{r}, t)$ at each point in space. We now review this approach and then develop the consequences of the model in the remainder of this paper.

Consider a large particle describable roughly as a sphere of radius R. Surface free energy will cause this particle to have an equilibrium monomer concentration

a)Supported in part by grants from the National Science Foundation and the Petroleum Research Fund.
b)Department of Chemistry.
c)Western Electric, Research Laboratories, New Jersey.
d)Department of Mathematics.
e)Department of Geology.
f)A. P. Sloan Fellow, 1980–1982.

 0021-9606/83/031293-19$2.10

C^{eq} that depends on R. For large R, $C^{eq}(R)$ is a monotonically decreasing function. Hence, if a large particle is near a small one it will grow at the expense of the latter. This competitive growth kinetics causes the typical particle size to increase in any domain of space. This cascade to larger particle sizes is called ripening.[10] Because of ripening, small particles in any given domain tend to be eliminated. The size of particles is also limited from above by virtue of the fact that particles beyond a given size have not had time to grow. Thus, we arrive at a picture such that in any small spatial domain, c_n (as a function of n) is peaked at some value $n^*(\mathbf{r}, t)$ in the post nucleation regime.

1. Competitive particle growth

Let $R(\mathbf{r}, t)$ denote the radius of the (assumed spherical) n^* particle. Because $C^{eq}(R)$ depends on R, we expect that if $R(\mathbf{r}, t)$ is higher in one region than its surroundings, then the maximum in R will grow and cause dissolution in its surroundings. This will in turn induce satellite maxima in R further away from the original R maximum. This scenario provides a mechanism of spontaneous pattern formation in precipitating systems. It has been tested experimentally using PbI_2 sols in agar.[7,8]

2. A simple mathematical model

Since the particle size distribution c_n tends to peak around n^* corresponding to a particle radius R, we approximate the $\mathbf{c} = (c_1, c_2, \ldots, c_n, \ldots)$ description by the concentration $C(\mathbf{r}, t)$ of the monomer and the local average particle size $R(\mathbf{r}, t)$. We take $R(\mathbf{r}, t)$ to satisfy

$$\frac{\partial R}{\partial t} = \frac{K}{\rho}[C - C^{eq}(R)], \tag{II. A3}$$

where ρ is the molar density of the solid and the rate parameter K may depend on R. In setting forth Eq. (II. A3), we assume that the precipitate particles are sufficiently large that their diffusion coefficient is small. This would be quite reasonable for a gel experiment. Simple considerations of conservation of mass lead to an evolution equation for C:

$$\frac{\partial C}{\partial t} = D^2 C - n\rho \frac{\partial}{\partial t}(\tfrac{4}{3}\pi R^3) + \frac{qW}{\epsilon} . \tag{II. A4}$$

We have assumed that after the nucleation phase is over, and coarsening has narrowed the particle size distribution, the number density n of precipitate particles is time independent. The term qW/ϵ represents a source of monomer and is written in that form for reasons that shall be clarified in Sec. III B below. After specifying qW/ϵ, and n Eq. (II. A3, 4) constitute a self-consistent model of post nucleation and post local coarsening evolution. Our objective is to show that this simple model can explain a host of spontaneous precipitation patterning phenomena. This will serve both to underscore our overall physical picture and justify further work on the more accurate (and exceedingly more technically complicated) particle growth model of Eqs. (II. A1) or (II. A2) as discussed in Ref. 9.

B. Characteristic lengths and times; Dimensionless variables

We introduce characteristic values of lengths, times, and concentrations so as to extract some of the basic physics from the problem. We find that only two dimensionless combinations of system parameters differentiate all systems. It shall be assumed henceforth that the equilibrium concentration $C^{eq}(R)$ takes the commonly used form

$$C^{eq}(R) = C^{eq}(\infty)\left[1 + \frac{2\Gamma R^2}{2R^3 + R_c^3}\right], \tag{II. B1}$$

$$\Gamma = 2\gamma_\infty / \rho v R T , \tag{II. B2}$$

where R_c, γ_∞, ρ, v, R, and T are the critical radius, surface tension of a flat crystal surface, crystal molar density, a stoichiometric coefficient, the gas constant and the absolute temperature, respectively.

The analysis proceeds by defining a typical particle radius $\bar{R}$ and particle number density $\bar{n}$. A typical value of the concentration is $C^{eq}(\infty)$. We also introduce a characteristic time $\bar{t}$ and length L and, in the course of our analysis, shall obtain a relation between the other system parameters and the latter. New dimensionless quantities are defined as follows:

$$C = C^{eq}(\infty)[1 + s], \quad R = \bar{R}\Psi , \quad \mathbf{r} = L\boldsymbol{\xi} ,$$
$$t = \bar{t}\tau , \quad n = \bar{n}\nu . \tag{II. B3}$$

With these definitions, Eqs. (II. A3) and (II. A4) become

$$\frac{\partial \Psi}{\partial \tau} = \frac{\bar{t} K C^{eq}(\infty)\Gamma}{\bar{R}^2 \rho}\left[\frac{\bar{R}s}{\Gamma} - g(\Psi, \Psi_c)\right] , \tag{II. B4}$$

$$\frac{\partial s}{\partial \tau} = \frac{D\bar{t}}{L^2}\nabla_{\xi}^2 s - \Psi^2 G\nu \frac{\partial \Psi}{\partial \tau} + \frac{q\bar{t}W}{\epsilon C^{eq}(\infty)} , \tag{II. B5}$$

where G is the ratio of a typical molar density of material in precipitate to that in solution, i.e.,

$$G \equiv \frac{4\pi \bar{R}^3 \rho \bar{n}}{C^{eq}(\infty)} . \tag{II. B6}$$

The function g, shown in Fig. 1(a), is defined by

$$g(\Psi, \Psi_c) \equiv \frac{2\Psi^2}{2\Psi^3 + \Psi_c^3} , \tag{II. B7}$$

where $\Psi_c = R_c/\bar{R}$. All system parameters vanish from Eq. (II. B4) if we define $\bar{t}$ by setting the coefficient in front of the parenthesis equal to unity and define a new "scaled supersaturation" σ: taking K constant we have

$$\bar{t} = \frac{\bar{R}^2 \rho}{K C^{eq}(\infty)\Gamma} , \tag{II. B8}$$

$$\sigma = \bar{R}S/\Gamma . \tag{II. B9}$$

With this, Eqs. (II. B4) and (II. B5) become

$$\frac{\partial \Psi}{\partial \tau} = \sigma - g(\Psi, \Psi_c) , \tag{II. B10}$$

$$\frac{\partial \sigma}{\partial \tau} = \frac{D\bar{t}}{L^2}\nabla_{\xi}^2 \sigma - \Psi^2 \beta\nu \frac{\partial \Psi}{\partial \tau} + \frac{\beta q w}{\epsilon} , \tag{II. B11}$$

where

$$\beta \equiv \bar{R}G/\Gamma , \tag{II. B12}$$

$$w \equiv \bar{R}\bar{t}\, W / C^{eq}(\infty)\Gamma\beta . \tag{II. B13}$$

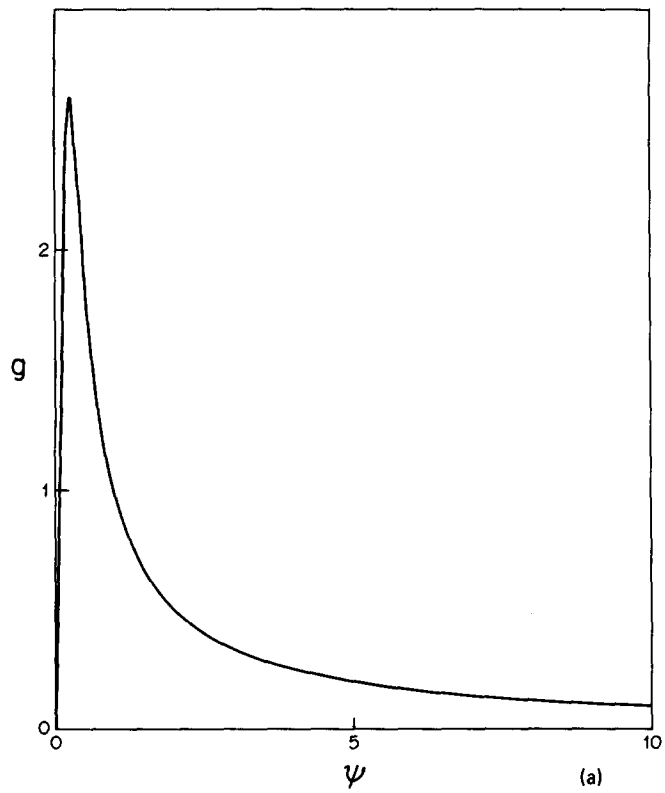

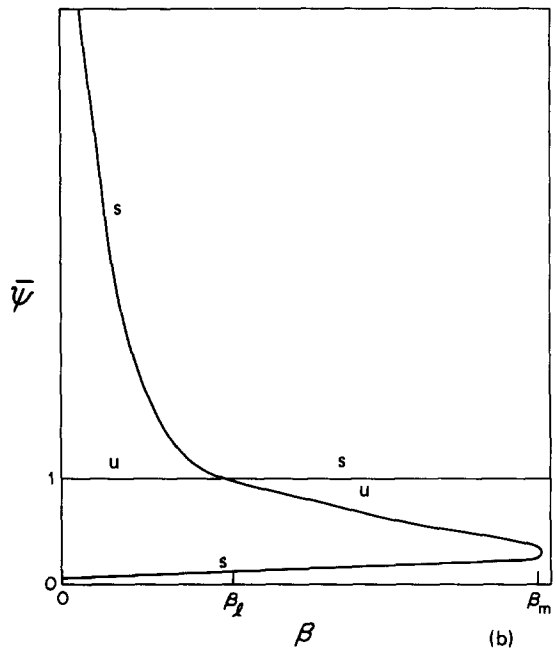

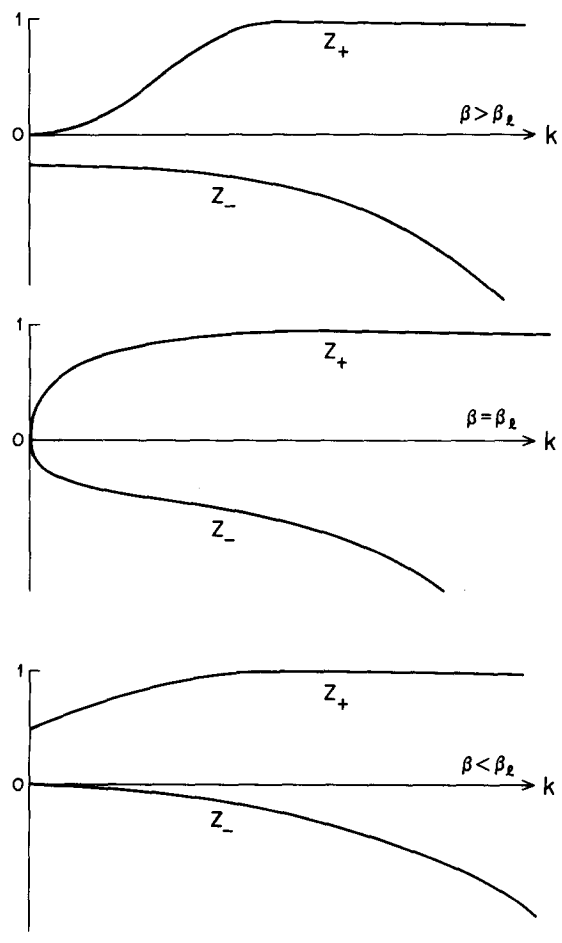

FIG. 1. (a) Normalized supersaturation function $g(\Psi)$ as a function of the ratio of particle radius to the typical particle radius ($\Psi = R/\bar{R}$). In most experimental situations the typical particle size is much larger than the critical radius so that $\Psi_c \ll 1$. In the simulations carried out in the figures to follow, this was the case. Hence the maximum of g (that occurs at about Ψ_c) is far to the left of the range of particle sizes of interest in the experiment. In this figure $\Psi_c = 0.25$. (b) States of the uniform sol as described by solutions of Eq. (II.C4) The labels "s" and "u" indicate the stability of sol states with respect to uniform perturbations. Stability with respect to patterned perturbations is discussed in Sec. II C. (c) Dependence of the stability eigenvalues $z_\pm(k)$ given in Eq. (II.C8) for the $\bar{\Psi} = 1$ state. Note that in all cases the branch z_+ is positive for all k values, indicating instability to pattern formation without giving any information about a preferred length for the pattern.

Finally, the characteristic length L is defined such that $D\bar{t}/L^2=\beta$. Thus, we obtain

$$L=\left(\frac{D}{4\pi\bar{R}^2\bar{n}K}\right)^{1/2} . \tag{II.B14}$$

With this, Eq. (II.B11) becomes

$$\frac{1}{\beta}\frac{\partial\sigma}{\partial\tau}=\nabla^2\sigma-\Psi^2\nu\frac{\partial\Psi}{\partial\tau}+\frac{qw}{\epsilon} . \tag{II.B15}$$

Here and henceforth we shall drop the subscript ξ from the Laplacian.

In the absence of the source (w) term, the system dynamics Eqs. (II.B10) and (II.B15) are characterized by two parameters β and Ψ_c. In most cases of interest here $\Psi_c=R_c/\bar{R}$ will be small—i.e., particles are much larger than the critical particle of radius R_c, and hence only one parameter β is the dimensionless combination of $C^{eq}(\infty)$, K, Γ, D, $\bar{n}$, and $\bar{R}$ that differentiates between systems.

C. States and stability of a uniform sol

The uniform sol is found to have multiple possible states of existence in the present theory. We examine these states and their stability and discuss the structural stability of the model.

1. Multiple uniform sol states

In the present model, the uniform static sol is specified by, letting a superscript "–" indicate a uniform sol state

$$\bar{\sigma}=g(\bar{\Psi}) . \tag{II.C1}$$

A second equation is obtained by combining Eqs. (III.B10) and (III.B15) to obtain

$$\frac{d}{d\tau}\left(\sigma+\frac{\beta}{3}\Psi^3\right)=0 \text{ for a uniform system} . \tag{II.C2}$$

Thus the bracketed quantity is a constant of the motion for a uniform sol. This constant, denoted σ_T, is simply the total amount of material in either particles or scaled supersaturation. Thus, we have

$$\bar{\sigma}+(\beta/3)\bar{\Psi}^3=\sigma_T . \tag{II.C3}$$

Combining Eq. (II.C1) and (II.C3) we get

$$g(\bar{\Psi})+(\beta/3)\bar{\Psi}^3=\sigma_T . \tag{II.C4}$$

Recall that β contains a dependence on the typical particle radius $\bar{R}$. Thus, with no loss of generality, we can assume that Eq. (II.C4) has one solution with $\bar{\Psi}\equiv 1$. The corresponding value of σ_T, σ_{T1}, is given by

$$\sigma_{T1}=g(1)+\beta/3 , \tag{II.C5}$$

We now investigate the possiblity of other solutions $\bar{\Psi}$, satisfying

$$g(\bar{\Psi})+(\beta/3)\bar{\Psi}^3=g(1)+\beta/3 , \tag{II.C6}$$

that may also exist consistent with a total material content $\sigma_T=g(1)+\beta/3$. The solutions of Eq. (II.C6) are indicated in Fig. 1(b). Notice that in the interval $0<\beta<\beta_m$ our model predicts the existence of three uniform sol states. Thus, in the range

$$g(1)<\sigma_T<g(1)+\beta/3 \tag{II.C7}$$

our model predicts multiple possible sol states for a given total material content.

2. Stability of the uniform sol

The realization of the uniform sol in a physical system depends on its stability. We test this via the usual small amplitude stability theory. Letting – indicate the uniform sol and $\sigma=g(\bar{\Psi})+\delta\sigma$, $\Psi\equiv\bar{\Psi}+\delta\Psi$, we find solutions $\delta\Psi$, $\delta\sigma$ for small perturbations in the form $\exp[z(k)\tau+ik\xi]$ where $z(k)$ is one of the following:

$$z_\pm(k)=-\tfrac{1}{2}[\beta(k^2+\bar{\Psi}^2)+\dot{g}] \pm\tfrac{1}{2}\sqrt{[\beta(k^2+\bar{\Psi}2)+\dot{g}]^2-4\beta\dot{g}k^2} , \tag{II.C8}$$

where $\dot{g}=dg/d\Psi$. For small k perturbations, we see that

$$z\underset{k\to 0}{\sim}0, \quad -\beta\bar{\Psi}^2-\dot{g} . \tag{II.C9}$$

The eigenvalue zero corresponds to the conservation law (II.C2). The other eigenvalue determines the stability of the sol to uniform perturbations. The results are shown in Fig. 1(b). There is an exchange of stability at the point β_1, where the upper solution crosses the line $\bar{\Psi}=1$. For $\Psi_c\ll 1$, $\beta_1(\Psi_c\ll 1)\sim 1$.

For patterned ($k\neq 0$) perturbations we must use Eq. (II.C8). States with $\dot{g}>0$ are always stable. The dependence of the branches $z_\pm$ on k for the $\bar{\Psi}=1$ state is shown in Fig. 1(c). Since z_- is monotonically increasing with k, the system is seen to be unstable to pattern formation although no preferred pattern length is indicated. For the larger β dependent state shown in Fig. 1(b), the dependence of the stability eigenvalue is similar to that shown in Fig. 1(c), except that the inequalities on β are reversed.

In conclusion, the stability analysis indicates that there exists a tendency for pattern formation in a uniform sol. However, to determine the length scale of the patterns we require a nonlinear analysis.

D. Numerical simulation of spontaneous pattering in an aging sol

1. Definition of the problem

We have undertaken a series of numerical simulations of the dynamics of an aging sol described by Eqs. (II.B10) and (II.B15) without the source term qw/ϵ: thus, the calculations were based on the following model:

$$\frac{\partial\Psi}{\partial\tau}=\sigma-g(\Psi) , \tag{II.D1}$$

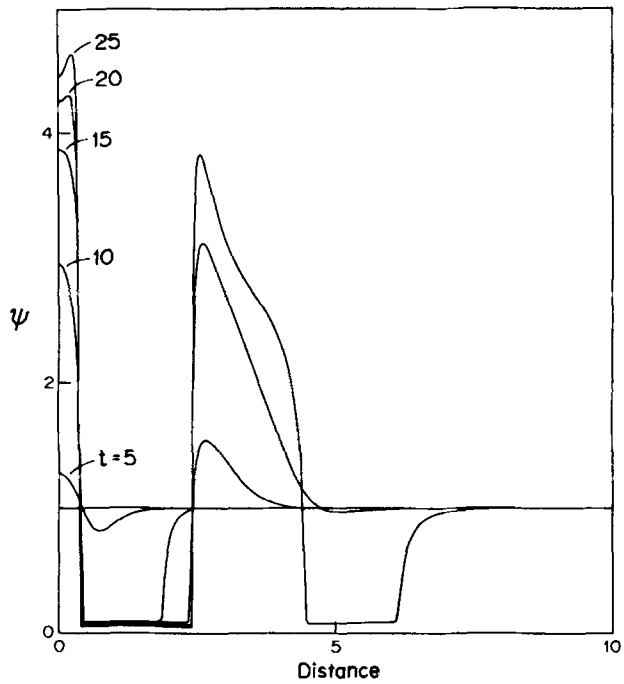

FIG. 2. Simulation of the growth of an initial bump and subsequent satellite induction. The initial sol was, by definition, at $\Psi \equiv 1$ with a small bump near the left-hand wall (the initial bump is essentially imperceivable on the scale of the graph). The first satellite develops at about 2.55. Note also that the initial bump is tending to split into a doublet (since the no flux boundary conditions allow one to reflect the profiles about the origin). The parameter values used were $\beta = 0.1$ and $\Psi_c = 0.25$.

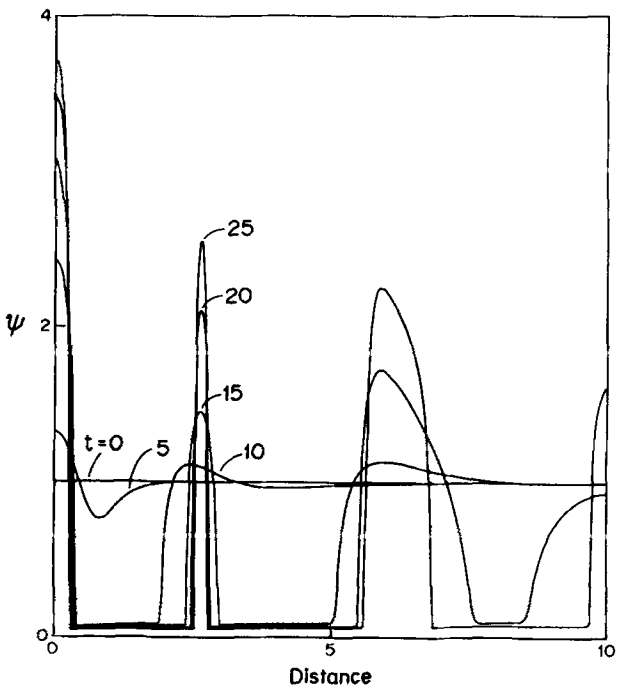

FIG. 3. Same as Fig. 2 except $\beta = 1.0$. Note the induction of multiple satellites. The first satellite has an asymptotic maximum at about 2.6. Unlike the case $\beta = 0.1$ of Fig. 2 there seems to be no tendency for the initial bump to split into a doublet.

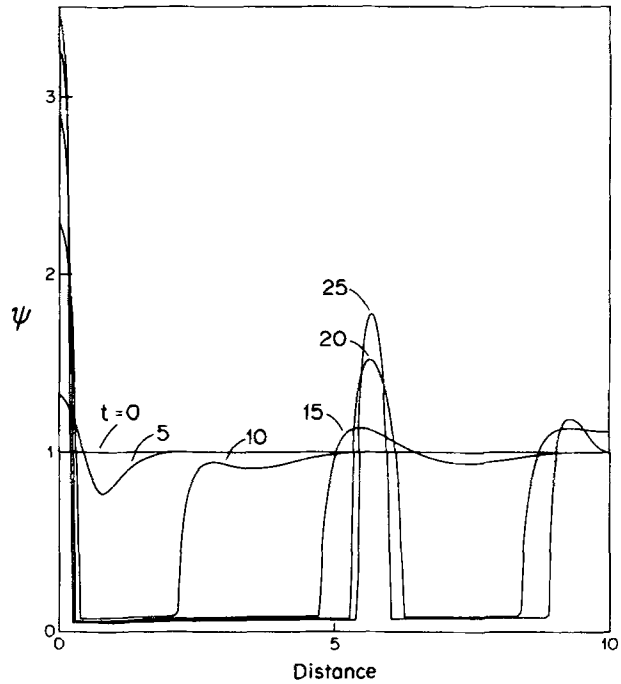

FIG. 4. Same as in Fig. 3 except that $\beta = 100$. At these high values of β the first satellite never quite matures—i.e., grows larger than the initial sol size $\Psi = 1$. However, note that the presumptive first satellite does attempt to develop at about 2.7, surprisingly very close to the first satellite induction distance for the $\beta = 0.1$, 1.0 cases of Figs. 2 and 3. This dramatic invariance is discussed further in Sec. II D. Since the first satellite is represented we see the phenomenon of period doubling for large β.

$$\frac{1}{\beta}\frac{\partial \sigma}{\partial \tau} = \frac{\partial^2 \sigma}{\partial \xi^2} - \Psi^2[\sigma - g(\Psi)] \,. \qquad \text{(II.D2)}$$

The equations were solved using standard iterated backward difference techniques.[12] The system consisted of a one-dimensional tube of length L_T. At boundaries $\xi = 0$, L_T, fluxless conditions were imposed, i.e., $\partial\sigma/\partial\xi = 0$ at $\xi = 0, L_T$. Note that in Eqs. (II.C1) and (II.C2) and henceforth, we repress the Ψ_c dependence of g.

2. *Satellite induction and its characteristic length*

In this series of simulations, we investigated the growth of satellite maxima in R induced by an initial bump. All simulations were carried out for fairly coarse sols, i.e., $\Psi_c = 0.2$ or 0.25 for which $g(\Psi)$ is shown in Fig. 1(a).

The most striking feature of these simulations is that over the range $0.01 \leq \beta \leq 100$ tested (see Figs. 2–5), it was found that the first satellite induction distance was almost constant at a value $\xi_1 \approx 2.7 \approx e$ (the natural logarithmic base). This implies that for a sol the satellite induction length $L_1 = \xi_1 L$ is approximately given by [see Eq. (II.B14)]

$$L_1 \approx \left(\frac{De^2}{4\pi R^2 nk}\right)^{1/2} \,. \qquad \text{(II.D3)}$$

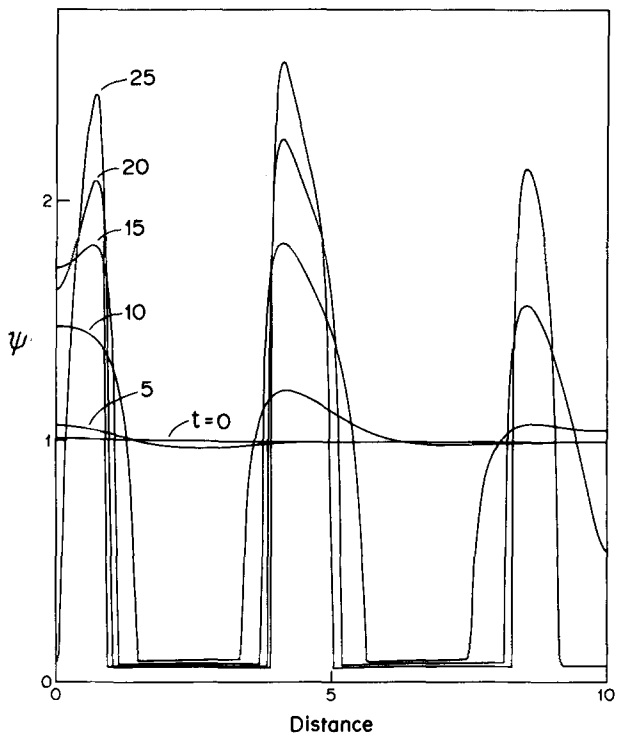

FIG. 5. Same as Fig. 3 except that the initial bump is taken to have a width comparable to the first satellite induction length, i.e., we took $\Psi(\xi,0)=i+0.01\exp[-(\xi/2)^2]$. Note that the central maximum breaks up into a doublet and in the process makes the average separation between the maximum of the doublet and the first satellite and their mirror images about 2.7, the invariant first satellite induction length.

This first satellite induction length law is not limited to a small amplitude analysis and is very surprising. The small amplitude analysis of Sec. IIC yields no characteristic length since it was found that the linear stability theory implies that under spontaneous pattern formation conditions, all wavelength perturbations grow—see Fig. 1(c). Thus, this pattern length is a strictly nonlinear interaction of the Fourier modes in the problem.

The detail features of the evolution do depend quite strongly on β however. We see in Fig. 2 that for small β, peaks tend to split up into secondary peaks. In Fig. 4, we see that the original peak has started to split into a doublet (think of the picture continued for $\xi<0$ and reflected about $\xi=0$) before the second satellite has formed. For large β, we see the very interesting effect of apparent satellite induction length doubling. In Fig. 5., the first satellite never grows above the average sol size and eventually disappears as the second satellite matures. However, note that the putative first satellite does attempt to rise at its usual location ξ_1, essentially independent of β. In Fig. 3 we see the clear formation of second and third satellites.

In Fig. 5 we investigate the effect of an interference between the initial bump shape and the first satellite. In that figure we took

$$\Psi(\xi,0)=1+0.01e^{-(\xi/2)^2},$$
$$\sigma(\xi,0)=g[\Psi(\xi,0)]. \qquad \text{(II. D4)}$$

The system is seen to attempt to find its characteristic length by splitting the central peak while inducing a satellite. Considering the profile to be reflection symmetric about $\xi=0$ we see that the average distance between the four central peaks—the central doublet and the satellite and its mirror image—is close to ξ_1.

3. *Random initial data*

A macroscopically "uniform" sol actually has slight random deviations in local average particle radius. Thus, since the uniform sol is unstable, we expect the small deviations from uniformity to grow and, because of diffusion, maxima and minima will interact. Results of simulations of this type are shown in Figs. 6 and 7. For large β, we expect that since the first satellite does not mature, the average pattern length for long times will be larger than for smaller β. This effect is seen clearly in Figs. 6 and 7.

Experiments on initially uniform PbI_2 sols show that the uniform state is indeed unstable and that in the aging process the uniform state makes the transition to macroscopic patterns as predicted in Figs. 6 and 7. Since these patterns occur post nucleation and in the absence of cross diffusion, they cannot be explained via the Ostwald–Prager theory.

4. *Secondary banding*

Secondary banding is the development of bands from an original precipitation band that occurred in an interdiffusion, Liesegang experiment. Since these bands arise in the wake of the moving precipitation reaction, they do not appear to involve nucleation and cross diffusion. Hence, the Ostwald–Prager mechanism cannot explain them.

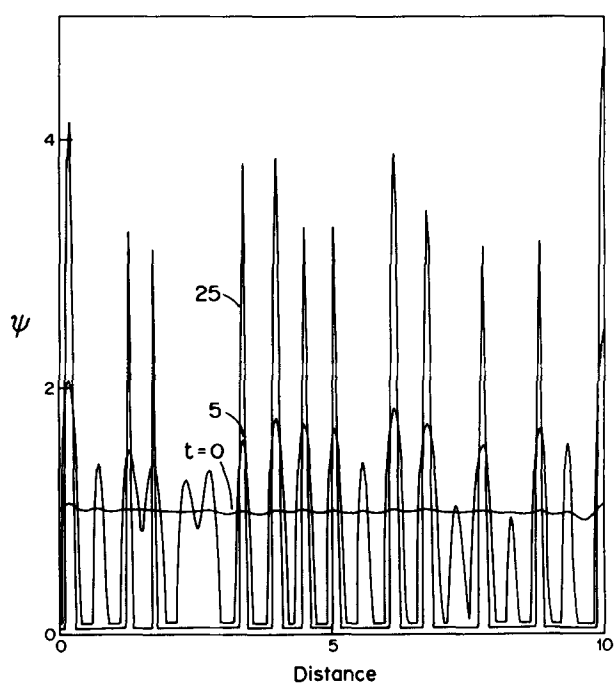

FIG. 6. Evolution of a small initially random variation of sol coarseness into a macroscopic pattern for parameter values $\beta=0.5$, $\Psi_c=0.25$.

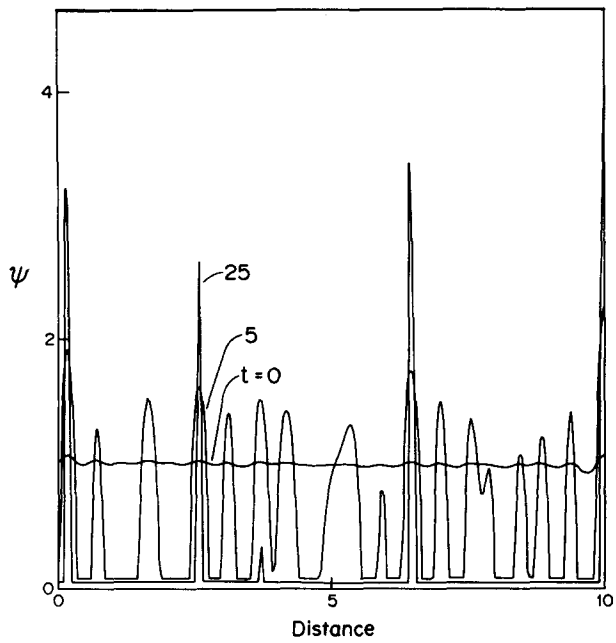

FIG. 7. Same as Fig. 6 except that $\beta = 100$. Note that the length scale between surviving maxima for a given time is much longer than the case in Fig. 6.

We have carried out numerical simulations of the competitive growth equations (II.C10) and (II.C15) to describe the evolution of a single band. In Figs. 8 and 9 we see the results. A gradient of particle size across the band induces smaller scale "secondary" banding.

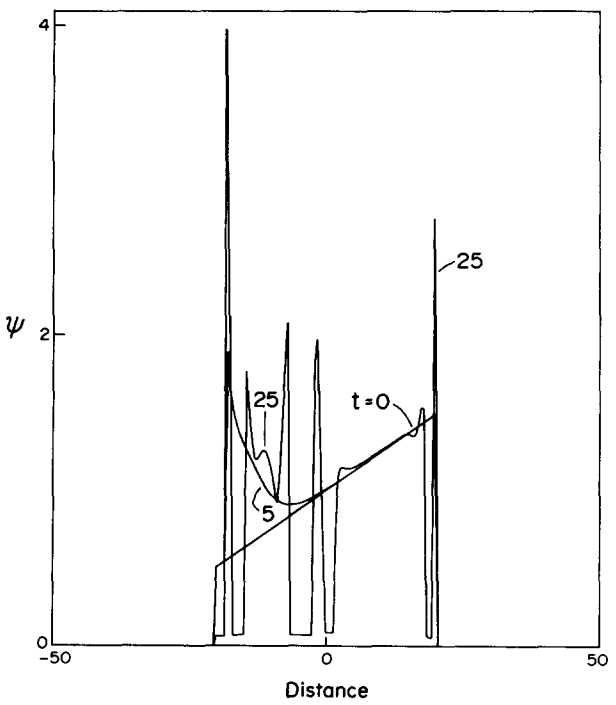

FIG. 8. Evolution of an initial band into secondary bending as simulated via the competitive particle dyanmics of Eqs. (II.D1) and (II.D2). Notice the interesting flip–flop that occurs in that the particles in the band at the end of the profile where the particles were initially smallest becomes the coarsest. Parameter values were $\beta = 1$, $\Psi_{cl} = 0.2$.

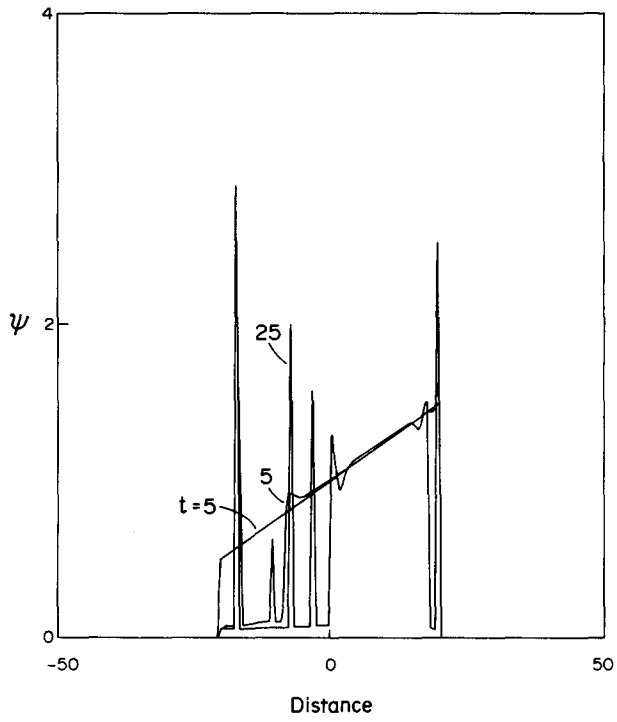

FIG. 9. Same as in Fig. 8 except that $\beta = 10$. Note that the left-hand band represses the formation of the first presumptive satellite as expected from the results of Fig. 4 where the length doubling for large β is also observed.

The results show a number of interesting features whose occurrence and properties depend on the value of β. In all cases tested the largest maximum in dimensionless particle radius Ψ arose at the end of the original band where Ψ was initially smallest. This reversal happens because when Ψ is smaller the surface tension mediated competitive dynamical feedback is stronger. In the case of larger β values, the period doubling phenomenon appears to be operative in annihilating the second band from the left before it came to maturity. The spacing of the secondary bands is on the order of the satellite induction length (or an integer multiple of it) but the original overall Ψ gradient appears to lead to minor deviations from it.

5. *Two sol junction experiment*

If two gels with uniform sols of different particle size are joined, we expect from the satellite induction simulations, that banding will be induced in the two gels. Simulations of this effect for three different values of β (= 0.1, 1, and 10) are shown in Figs. 10–12, respectively. The results are quite well explained by the invariant induction length hypothesis and the experience obtained from the satellite induction simulations. Variables in Figs. 10–12 are defined with $\bar{R}$ being the initial particle radius in the right half of the system. This predicts, according to the expression (II.C3), that the pattern length to the left is half that to the right of the junction, as it clearly is. Also note that high β systems tend to skip the first satellite—as expected from the satellite induction simulations in Sec. II.C2 above.

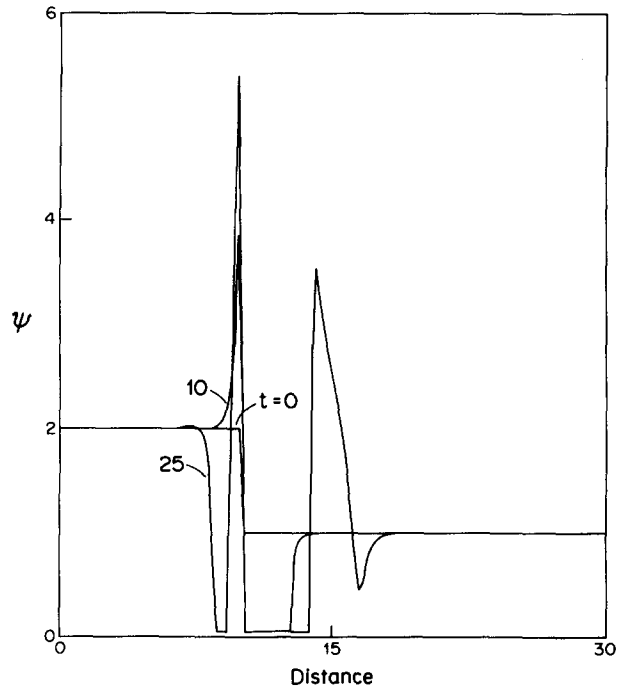

FIG. 10. Numerical simulation via Eqs. (II.D1) and (II.D2) of an experiment wherein a coarser sol (left) was interfaced with a finer one (right). The experiment is seen to result in banding in both media. Parameters used were $\beta = 0.1$, $\Psi_c = 0.2$ with $\Psi(\xi, 0)$ as shown and $\sigma(\xi, 0) = g[\Psi(\xi, 0)]$.

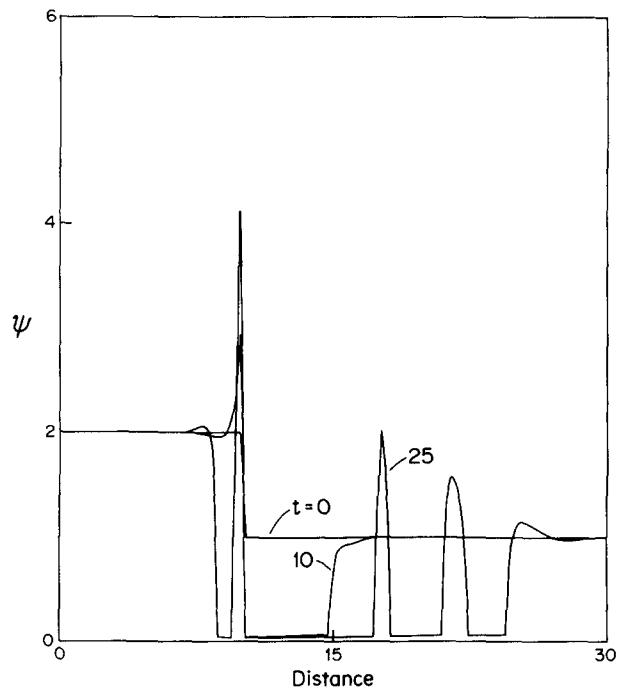

FIG. 12. Same as Fig. 10 except $\beta = 10$. Notice in the finer sol region the first satellite is repressed as expected from the satellite induction simulations as in Fig. 4.

E. Arbitrarily spaced arrays of rectangular teeth

The uniform sol is not the most general time independent solution of the competitive particle growth equations (II.D1) and (II.D2). Let σ^* be a constant between zero and the maximum value g_m of $g(\Psi)$

$$0 < \sigma^* < g_m \,. \tag{II.E1}$$

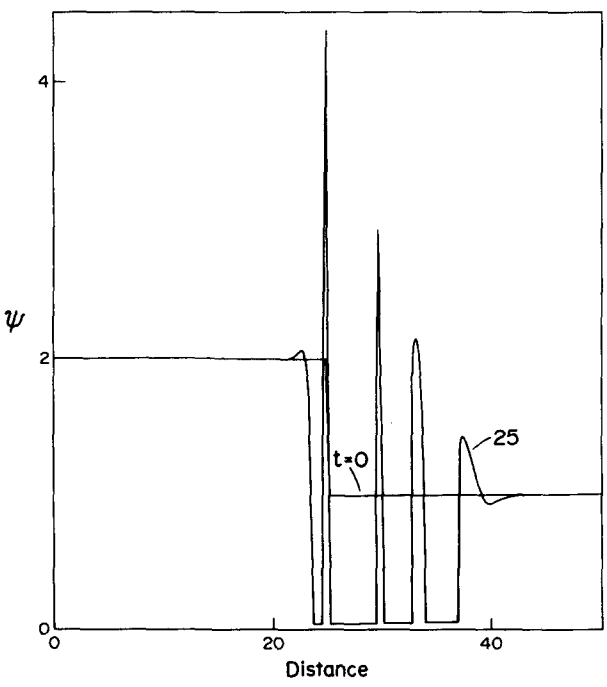

FIG. 11. Same as Fig. 10 except $\beta = 1$.

Then from Fig. 1(a) we see that the equation

$$g(\Psi) = \sigma^* \tag{II.E2}$$

has two solutions that we denote $\Psi_1(\sigma^*)$, $\Psi_2(\sigma^*)$. Let $\theta_{ij}(\xi) = 1$, $\xi_i < \xi < \xi_j$; $\theta_{ij}(\xi) = 0$ otherwise for a series of positions. Then

$$\Psi = \Psi_1 + (\Psi_2 - \Psi_1) \sum_{i,j} \theta_{ij}(\xi) \,, \tag{II.E3}$$

$$\sigma = \sigma^*$$

satisfies Eqs. (II.D1) and (II.D2). For most systems, one of the particle sizes, Ψ_2 say, will be much less than the other, Ψ_1. We expect that the rectangular sawtooth patterns [Eq. (II.E2)] are not stable to perturbations in the teeth heights about Ψ_1. The rate of increase in the height difference between neighboring teeth should be proportional to the inverse of the square of the distance separating them. This leads to a cascade up in length scale as neighbors compete and smaller ones are annihilated. In the random initial condition and many simulations to follow this competition of maxima is observed. Note that particles between bands will not be completely dissolved but the size will bottom out at a value close to a value of the solution of the equation $g(\Psi) = g(\Psi_n)$ where Ψ_n is the size of the neighboring maximum.

F. The greedy giant catastrophe

It is often observed that between bands in the cross diffusion experiment, large isolated crystals appear. Similar isolated crystals are found in the essentially precipitate free areas that occur when a uniform sol ages into a mottled pattern.[8] We term these isolated crystals "greedy giants," because they arise out of the

competitive advantage that crystals in the tail of the size distribution possess due to the surface tension mechanism. Indeed, these isolated giants grow faster when the more typically sized crystals are being coherently dissolved out because of a neighboring average particle size maximum.

The large wave vector k behavior of the stability eigenvalues discussed in Sec. IIC (such that z approaches a positive constant as $k \to \infty$) is due to this greedy giant phenomenon. A small perturbation in R in the form of a localized maximum crudely models a crystal that is larger than those around it. However, this is not a particularly accurate description, mainly due to the fact that diffusion cannot occur inside an actual particle. The occurrence of greedy giants is a statistical question, requiring the introduction of a particle size distribution function[9] and will not be pursued further here.

III. CROSSFLUX KINETICS

A. Experiments on the oxalic acid-gold system

Some old experiments on the formation of gold bands resulting from the cross diffusion of oxalic acid and gold[2] were repeated in our laboratory.[13] We cite some of the results here to set the stage for our subsequent model making.

Glass tubes were filled with agar or silica gel solutions of $AuCl_4^-$ ions. Oxalic acid solutions in water were imposed on top of the gels allowing the acid to diffuse into the gel. As the oxalic acid (denoted A) diffused into the gel, the $AuCl_4^-$ (denoted B) was reduced to gold atom (monomer, denoted C. The reduction process is characterized by the overall reaction

$$3A + 2B \to 2C + \cdots , \qquad \text{(III. A1)}$$

where the dots indicate other products that are not of interest here. To a very good approximation, Eq. (III. A1) is irreversible.

The advancement of oxalic acid into the Au^{3+} bearing gel is marked by a well-defined zone in which the yellow color due to Au^{3+} is absent. In the reduced (Au^{3+} free) zone a haziness appears somewhat behind the leading edge of that zone—see Plate I. The haze signals the presence of particles of diameter greater than the wavelength of visible light.

Banding is then observed to emerge out of the haze—i.e., the haze in the reducing zone breaks up into alternative bands of relative clear and precipitate laidened regions. This is in contradiction with the predictions of the Ostwald–Prager theory, wherein sequential nucleation and nuclei free zones are created.

To further investigate this point, we set up a light transmission experiment as follows: A tube developing banding was placed between a columated light beam and a light detector. The beam-detector couple was moved along the tube by computer controlled stepper motors. The data was digitized, stored and displayed as temporal sequences of transmitted light intensity as a function of distance along the tube at given times.

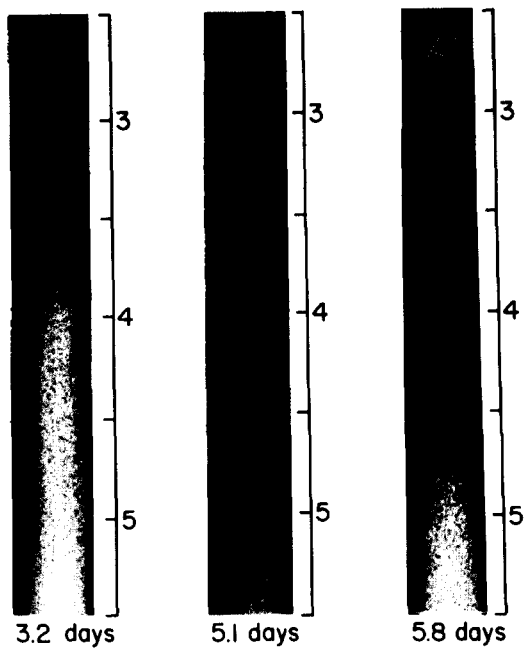

Plate I. Band formation resulting from the diffusion of oxalic acid into a gel solution of $AuCl_4^-$. The stoichiometry of the interdiffusion reaction leading to monomer production is summarized in Eq. (III. A1). Notice that a leading monotonic front of hazing forms well in advance of bands, ruling out the classic mechanism of Ostwald and Prager (Refs. 5 and 6). Banding of this type appears to be the result of the surface tension mediated instability of a uniform sol to pattern formation as described by the present theory. The experiment shown was carried out by placing a gel solution of $HAuCl_4$ in a test tube and superimposing a solution of oxalic acid. The one weight percent chlorauric acid gel solution was made by combining 8 ml of 1.075 g/cc sodium silicate solution, 15 ml of 0.6 M acetic acid, and 3 ml 0.2115 M $HAuCl_4$ and allowing the gel to set in the tube. The oxalic acid solution used was 0.22 M. The time indicates hours after imposition of the oxalic acid. Evolution took place in the dark (to avoid photochemical effects). The tubes were maintained vertical at all times. [Gravity is known to sometimes affect precipitation patterns (Ref. 20)].

(See Ref. 13 for more complete details and Ref. 20 for related work).

A telling sequence is shown in Plate II. A silica gel solution of 1% by weight $HAuCl_4 \cdot H_2O$ was allowed to interact with an 8% by weight superimposed solution of $H_2C_2O_4$. In plate II, we plot the fraction of light not transmitted f ($f = 1 - I/I_0$, I_0 = incident light intensity, I = transmitted intensity). This is a measure of the amount of precipitate contained in the tube (since I_0 is measured as the light transversing the precipitate free, $AuCl_4^-$ silica gel). A zone of hazing clearly precedes the domain where bands are emerging. The bands are seen to emerge from the unbanded sol. Note the interesting transition from the relatively narrowly spaced bands to the wider, smoother bands. This agrees well with the numerical simulations based on the competitive particle theory to be presented below. Other similar experiments presented in Ref. 13, the $AuCl_4^-$ tubes are prehazed with Au–sol by introducing a given amount of $H_2C_2O_4$ and similar banding to that of Plate II occurs. Thus, nucleation is not an integral part of the kinetics

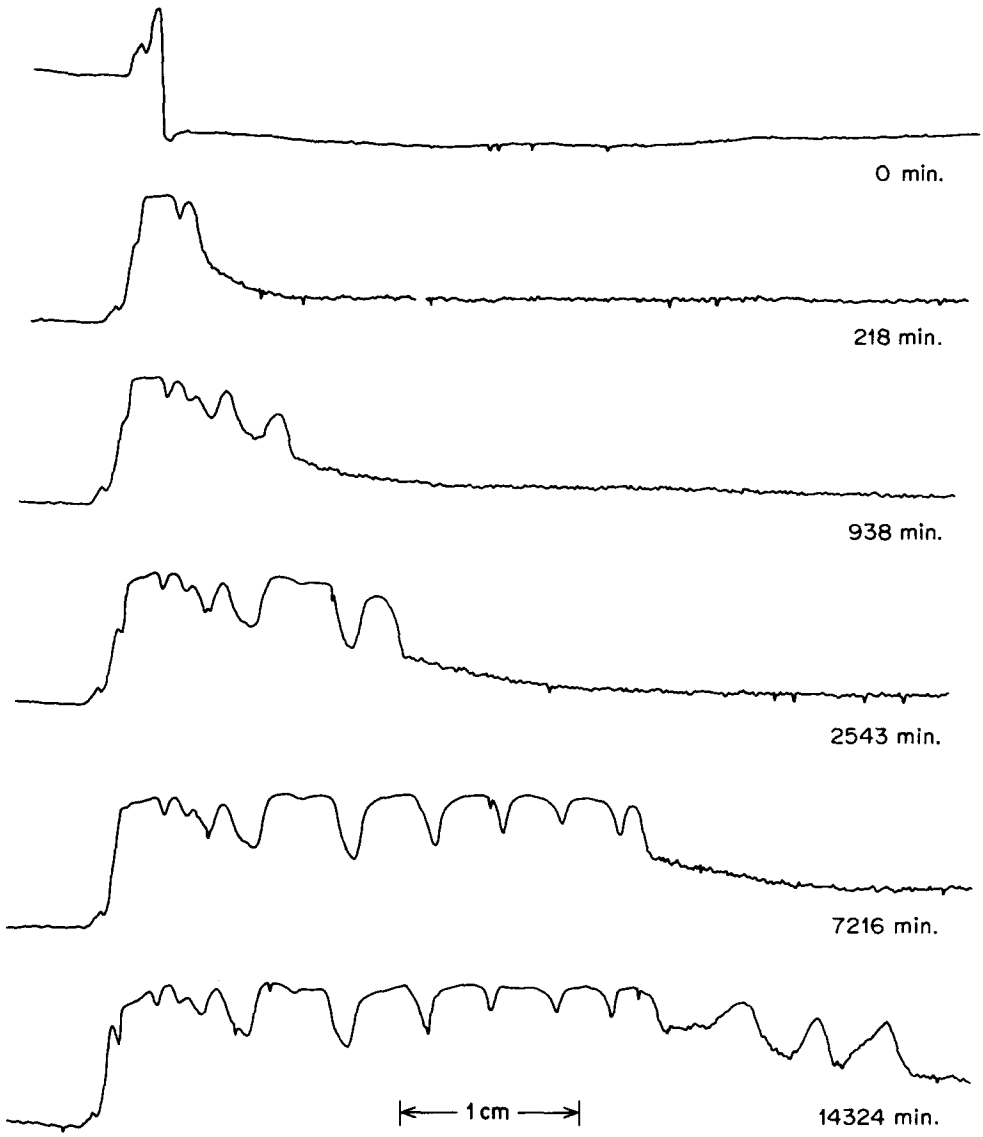

Plate II. Development of Au bands resulting from the infusion of a 2% by weight solution of $H_2C_2O_4$ into a 1% by weight solution of $AuCl_4 \cdot H_2O$ in silica gel. The quantity plotted is proportional to the percentage of light not transmitted $f = 1 - I/I_0$ where I is the light transmitted and I_0 is the light transmitted through the precipitate free gel solution. Thus f increases as the amount of precipitate. The distance shown is a 3 in. segment of the tube. The most important observation is that banding occurs in the zone behind the $H_2C_2O_6$ and nucleation fronts—i.e., the bands develop out of a pre-existing haze. The scan labeled 0 min is taken before the $H_2C_2O_4$ solution is superimposed. All other times indication the duration after $H_2C_2O_4$. (See Ref. 13 for further details.)

of band formation.

In the remainder of this section, we shall study the front of monomer Au production that drives the interdiffusion banding.

B. Creation of monomer

1. Basic equations

The interdiffusion of reductant and metal ion that produces metal monomer shall be generalized to the process

$$m\mathrm{A} + n\mathrm{B} \rightarrow q\mathrm{C} + \cdots \quad . \tag{III.B1}$$

The other products of this irreversible reaction are taken to be inert (with respect to pattern formation) and are neglected henceforth; m, n, q are stoichiometric coefficients. Assuming Eq. (III.B1) proceeds with rate $(1/\epsilon)/W$ (mol equivalents/volume time) we take the concentrations of A, B, and C to satisfy

$$\frac{\partial \mathrm{A}}{\partial t} = D_{\mathrm{A}} \frac{\partial^2 \mathrm{A}}{\partial x^2} - \frac{m}{\epsilon} W , \tag{III.B2}$$

$$\frac{\partial \mathrm{B}}{\partial t} = D_{\mathrm{B}} \frac{\partial^2 \mathrm{B}}{\partial x^2} - \frac{n}{\epsilon} W , \tag{III.B3}$$

$$\frac{\partial \mathrm{C}}{\partial t} = D_{\mathrm{C}} \frac{\partial^2 \mathrm{C}}{\partial x^2} + \frac{q}{\epsilon} W + H . \tag{III.B4}$$

The term H in Eq. (III.B4) indicates contributions from other reactions and precipitate particle growth. A factor $(1/\epsilon)$ has been added in Eqs. (III.B2)–(III.B4) to emphasize that in many cases, Eq. (III.B1) is fast and hence it is convenient to examine Eqs. (III.B2)–(III.B4) in the limit $\epsilon \ll 1$.

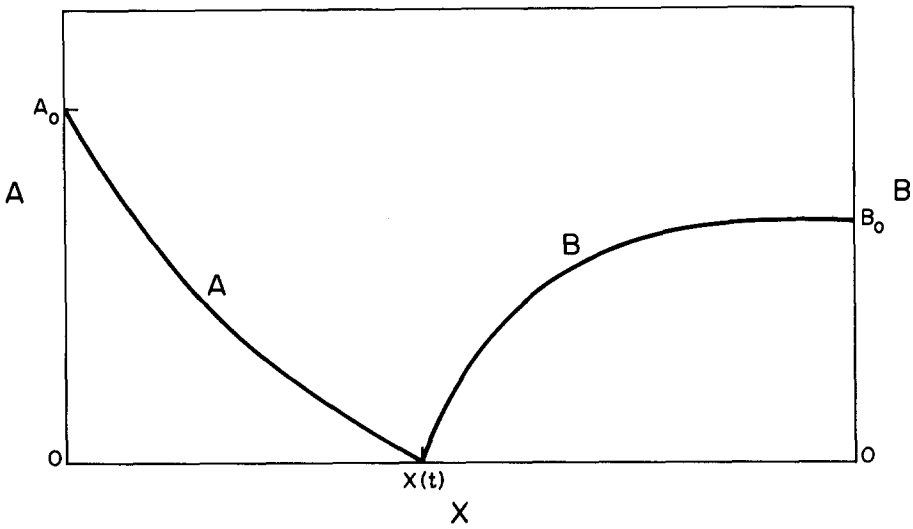

FIG. 13. Concentration profiles of cross diffusion experiment of species A moving into the B laden tube. The reaction $mA+nB \rightarrow$ products is considered fast. Hence there exists a moving interface at $X(t)$ where both A and B vanish. A is assumed fixed at the value A_0 at the left-hand boundary; B_0 is the value of B before A invasion.

The boundary conditions and initial data arising from the interdiffusion problem in an infinitely long tube located in $0 \le x < \infty$ are given by

$$A(0,t) = A_0, \quad A(x,0) = 0, \quad B(x,0) = B_0 , \tag{III.B5}$$

where A_0 and B_0 are constants.

2. *The moving boundary problem*

As $\epsilon \to 0$, we see from Eqs. (III.B2) and (III.B3) that A and B must vary rapidly in space or time unless W is small. This suggests that the limiting ($\epsilon \to 0$) profiles of A and B attain a form as in Fig. 13. This picture follows from the assumption that W must vanish if either A or B does and hence space is divided into an A-free region $x > X(t)$. a B-free region $0 \le x \le x(t)$, and a reaction interface where A and B meet, a small interval about $X(t)$ as observed in the oxalic acid–gold system.

In an earlier paper on the propagation of chemical waves, it was shown that problems of this type may be reduced to a Stefan moving boundary problem.[15,16] In this section, we apply this method to generate the moving boundary problem associated with Eqs. (III.B2) and (III.B5) and subsequently obtain an exact solution of this problem.

Since A vanishes for $x > X(t)$ and B vanishes for $0 \le x \le X(t)$, one finds upon eliminating W/ϵ from Eq. (III.B2) via Eq. (III.B3) that

$$\frac{\partial A}{\partial t} = D_A \frac{\partial^2 A}{\partial x^2}, \quad B = 0, \quad 0 \le x \le X(t) , \tag{III.B6}$$

$$\frac{\partial B}{\partial t} = D_B \frac{\partial^2 B}{\partial x^2}, \quad A = 0, \quad X(t) \le x < \infty , \tag{III.B7}$$

$$A[X(t),t] = B[X(t),t] = 0 . \tag{III.B8}$$

These equations and the data Eq. (III.B5) admit a solution on their indicated domains if the position $X(t)$ of the moving reaction interface is known.

Determination of $X(t)$ requires an additional condition—a Stefan condition—and we shall next obtain it by a more detailed examination of the system behavior in the vicinity of $X(t)$. To do so we introduce scaled variables

$$\zeta = [x - X(t)]/\epsilon^{\mu_1}, \quad A = \epsilon^{\mu_2}\hat{A}(\zeta,t) , \quad B = \epsilon^{\mu_3}\hat{B}(\zeta,t) . \tag{III.B9}$$

This scaling expands the spatial domain about the interface and also reflect the fact that A and B are small in this domain. The specific values of the exponents μ_1, μ_2, μ_3 follow from inserting this general scaling (i.e., using arbitrary powers of ϵ) and then determining which choices properly, as $\epsilon \to 0$, balance the relevant dominant process taking place in the interface. The latter are found to be a stoichiometric balance of A, B influx into the interface. Since the choice of exponents depends on the way in which W vanishes with A and B as the latter go to zero, we shall assume

$$W = kAB, \tag{III.B10}$$

where k(A, B) is a positive function that is nonzero as A, B $\to 0$, i.e.,

$$k(A,B) \underset{A,\,B\to 0}{\sim} k_0 > 0 . \tag{III.B11}$$

(More general cases such as $W = kA^\alpha B^\beta$ may also be analyzed by our method.) For Eq. (III.B10)

$$\mu_i = 1/3, \quad i = 1,2,3 \tag{III.B12}$$

is found to be the correct choice.

Using this scaling we obtain as $\epsilon \to 0$

$$D_A \frac{\partial^2 \hat{A}}{\partial \zeta^2} - mk_0 \hat{A}\hat{B} = 0 , \tag{III.B13}$$

$$D_B \frac{\partial^2 \hat{B}}{\partial \zeta^2} - nk_0 \hat{A}\hat{B} = 0 . \tag{III.B14}$$

Multiplying Eq. (III.B13) by n and Eq. (III.B14) by m, subtracting Eq. (III.B10) from Eq. (III.B11) and integrating over the interface, $-\infty < \zeta < +\infty$ for the scaled variable, we get

$$nD_A \frac{\partial \hat{A}}{\partial \zeta}(\zeta = -\infty, t) = -mD_B \frac{\partial \hat{B}}{\partial \zeta}(\zeta \to +\infty, t) , \tag{III.B15}$$

upon invoking $\partial\hat{A}/\partial\zeta(+\infty,t) = \partial\hat{B}/\partial\zeta(-\infty,t) = 0$. We note that from the definitions [Eq. (III.B7)] we have

$$\left(\frac{\partial A}{\partial x}\right)_t = \left(\frac{\partial \hat{A}}{\partial \zeta}\right)_t \tag{III.B16}$$

and similarly for B. We next take the matching conditions (see Refs. 15 and 16),

$$\lim_{x \to X(t)-0^+} \left(\frac{\partial A}{\partial x}\right)_t = \lim_{\zeta \to -\infty} \left(\frac{\partial \hat{A}}{\partial \zeta}\right)_t , \tag{III.B17}$$

$$\lim_{x \to X(t)+0^+} \left(\frac{\partial B}{\partial x}\right)_t = \lim_{\zeta \to +\infty} \left(\frac{\partial \hat{B}}{\partial \zeta}\right)_t . \tag{III.B18}$$

Here 0^+ is an infinitesimal positive number and $x \to X(t) \pm 0^+$ indicate taking the limit as x approaches $X(t)$ from the right and left, respectively. The required Stefan condition is then obtained by combining Eqs. (III.B12), (III.B14), and (III.B15) with Eq. (III.B13) and its B analog to find

$$nD_A\left(\frac{\partial A}{\partial x}\right)[X(t), t] = -mD_B\left(\frac{\partial B}{\partial x}\right)[X(t), t] . \tag{III.B19}$$

3. *Analytical solution of the Stefan problem*

Equations (III.B6)–(III.B8), and (III.B16) constitute a well posed Stefan problem. We now present an analytical solution of it. Since A and B are diffusing, we might expect that the interface behaves like a characteristic diffusion length. Thus, we conjecture

$$X(t) = \alpha\sqrt{t} \tag{III.B20}$$

for a yet unknown constant α. This suggests that a more natural spatial variable is a similarity variable[17]

$$\xi = \frac{x}{\sqrt{t}} . \tag{III.B21}$$

This approach turns out to be quite fruitful and we obtain an equation for α in the form

$$\omega\sqrt{D}e^{Da^2}\int_{a/\sqrt{D}}^{\infty} e^{-z^2}dz = e^{a^2}\int_0^a e^{-z^2}dz , \tag{III.B22}$$

where

$$D = D_A/D_B, \quad \omega = nA_0/mB_0 ,$$
$$\alpha = 2a\sqrt{D_A}. \tag{III.B23}$$

It is most convenient to calculate ω for various values of a and D. This is given in Fig. 14.

The concentration profiles are found to depend on the similarity variable ξ as follows:

$$A(\xi) = A_0 + 2\sqrt{D_A}A'\int_0^{\xi/2\sqrt{D_A}} e^{-z^2}dz , \tag{III.B24}$$

$$B(\xi) = 2\sqrt{D_B}B' e^{a^2}/D_B \int_{\alpha/2\sqrt{D_B}}^{\xi/2\sqrt{D_B}} e^{-z^2}dz . \tag{III.B25}$$

The constants A′ and B′ are given by

$$A_0 + 2\sqrt{D_A}A'\int_0^{\alpha/2\sqrt{D_A}} e^{-z^2}dz = 0 , \tag{III.B26}$$

$$nD_A A' e^{-\alpha^2/4D_A} + mD_B B' = 0 . \tag{III.B27}$$

Thus, we have a complete analytical solution of this cross diffusion Stefan problem.

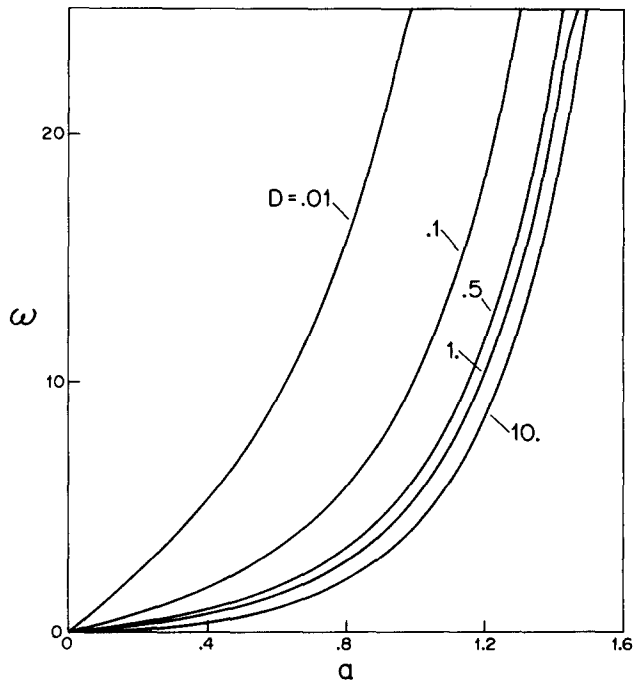

FIG. 14. Numerical solution of Eq. (III.B22) yielding scaled interface advancement rate a as a function of the composition variable ω at various values of diffusion coefficient ratio D (see Sec. III B for definitions).

C. The Rate of monomer production

The reaction interface wherein Eq. (III.B1) proceeds with appreciable rate is of a thickness that vanishes as $\epsilon \to 0$. Thus, the term qW/ϵ that represents the rate of monomer production in the continuity Eq. (III.B4) for the monomer concentration C should be a function that is high and narrowly peaked in the fast reaction ($\epsilon \to 0$) limit. We represent the qW/ϵ term by a delta function localized to $X(t)$ and with weight $N(t)$,

$$\frac{qW}{\epsilon} \underset{\epsilon \to 0}{\sim} N(t)\delta[x - X(t)] \tag{III.C1}$$

and use the asymptotic approximation, Stefan problem approach above to calculate $N(t)$.

Integration of Eq. (III.B25) in a small interval of width $2\epsilon^{1/3}\Delta$ centered on $X(t)$ we get, with $W = kAB$

$$N(t) \underset{\epsilon \to 0}{\sim} \frac{qk_0}{\epsilon}\int_{X-\epsilon^{1/3}\Delta}^{X+\epsilon^{1/3}\Delta} AB\,dx . \tag{III.C2}$$

Converting the integration variable to ζ and using Eq. (III.B9) we get

$$N(t) = qk_0\int_{-\Delta}^{\Delta} \hat{A}\hat{B}\,d\zeta . \tag{III.C3}$$

Using Eq. (III.B13) we get

$$N(t) = \frac{q}{m}D_A\int_{-\Delta}^{\Delta} \frac{\partial^2 \hat{A}}{\partial \zeta^2}_t d\zeta . \tag{III.C4}$$

Choosing Δ large enough so that $(\partial\hat{A}/\partial\zeta)$ at Δ is negligible we get (formally putting $\Delta \to \infty$)

$$N(t) = \frac{-q}{m}D_A\left(\frac{\partial \hat{A}}{\partial \zeta}\right)_t(-\infty, t) = \frac{-q}{m}D_A\left(\frac{\partial A}{\partial x}\right)_t[X(t), t] , \tag{III.C5}$$

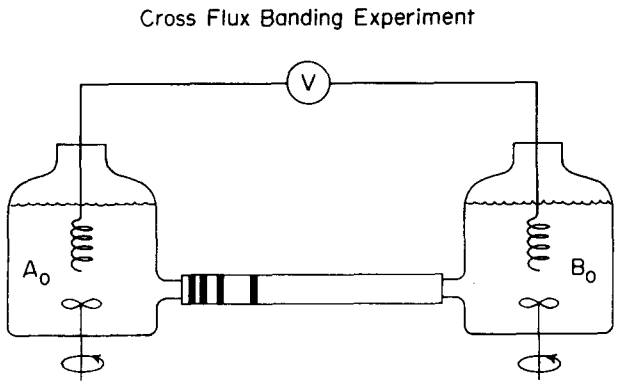

FIG. 15. Configuration for electroinfusion experiments.

where we have used Eq. (III.B17). Finally, invoking Eq. (III.B24) we get

$$N(t) = 2qa\mathrm{A}' e^{-a^2}/D_{\mathrm{A}}\sqrt{t} \equiv \Lambda t^{-1/2} . \quad \text{(III.C6)}$$

Note that as the interface advances into the system the rate of production decreases as $t^{-1/2}$. This is due to the fact that as the interface moves forward the concentration profiles of A and B become increasingly shallow and hence the rate of A and B flux to the reaction zone decreases.

D. Electrical field effects

When an electrical field is applied to an interdiffusion phenomenon, it has been found experimentally that the band spacing becomes constant.[14] Here we examine the effects of an applied field on an interdiffusion experiment in a manner analogous to the analysis of the previous two sections. Experimentally the situation we seek to model is described in Fig. 15 and its caption.

1. The constant velocity reaction interface

The effect of an electric field E (V/cm) is to modify Eqs. (III.B2) and (III.B3). Assuming the presence of a constant electric field E and a background electrolite (to eliminate the complexities of charge neutrality coupling[16]) we find

$$\frac{\partial \mathrm{A}}{\partial t} = D_{\mathrm{A}}\frac{\partial^2 \mathrm{A}}{\partial x^2} - \alpha\frac{\partial \mathrm{A}}{\partial x} - \frac{m}{\epsilon}W , \quad \text{(III.D1)}$$

$$\frac{\partial \mathrm{B}}{\partial t} = D_{\mathrm{B}}\frac{\partial^2 \mathrm{B}}{\partial x^2} - \beta\frac{\partial \mathrm{B}}{\partial x} - \frac{n}{\epsilon}W , \quad \text{(III.D2)}$$

$$\alpha \equiv z_{\mathrm{A}}\mathfrak{F}M_{\mathrm{A}}E, \quad \beta = z_{\mathrm{B}}\mathfrak{F}M_{\mathrm{B}}E . \quad \text{(III.D3)}$$

Here z_i and M_i ($i = \mathrm{A}, \mathrm{B}$) are the valences and mobility of species i and $\mathfrak{F}$ is Faraday's constant. The most profound effect of the electrical field is to allow for the possibility of constant velocity A–B interface propagation as follows. Let us assume that a transient phase, when the A–B interface has not yet moved in far from the end of the tube, has passed. Thus, the tube end is considered to be at $x = -\infty$. We now seek solutions that propagate with constant velocity and profile $\mathrm{A}(\phi)$, $\mathrm{B}(\phi)$ where ϕ is the coordinate system moving at velocity v with the interface,

$$\phi = x - vt . \quad \text{(III.D4)}$$

For these solutions, Eqs. (III.D1) and (III.D2) become

$$D_{\mathrm{A}}\mathrm{A}'' + (v-\alpha)\mathrm{A}' - \frac{m}{\epsilon}W = 0 , \quad \text{(III.D5)}$$

$$D_{\mathrm{B}}\mathrm{B}'' + (v-\beta)\mathrm{B}' - \frac{n}{\epsilon}W = 0 , \quad \text{(III.D6)}$$

where "′" indicates $d/d\phi$.

2. The advancement velocity

We may easily obtain an exact expression for v that depends only on the stoichiometry (i.e., on m, n). Eliminating W from Eqs. (III.D5) and (III.D6) we get

$$\left\{\frac{1}{m}[D_{\mathrm{A}}\mathrm{A}' + (v-\alpha)\mathrm{A}] - \frac{1}{n}[D_{\mathrm{B}}\mathrm{B}' + (v-\beta)\mathrm{B}]\right\}' = 0 . \quad \text{(III.D7)}$$

Clearly the quantity inside the braces is a constant of the motion. Let A^0 and B^0 be the values of $\mathrm{A}(-\infty)$ and $\mathrm{B}(+\infty)$, respectively. Then using the fact that $\mathrm{A}(+\infty) = \mathrm{B}(-\infty) = 0$, evaluating the braced quantity in Eq. (III.D7) at $+\infty$ and $-\infty$ and equating the results we get

$$v = \frac{\alpha \mathrm{A}^0/m + \beta \mathrm{B}^0/n}{\mathrm{A}^0/m + \mathrm{B}^0/n} . \quad \text{(III.D8)}$$

Thus, we see that if a wave exists, its velocity is proportional to the applied field and that it propagates into the B or A domains if the numerator of Eq. (III.D8) is $\gtrless 0$, respectively.

3. The rate of monomer production

The total rate of monomer production is qW/ϵ integrated from $-\infty$ to $+\infty$ for the wave. From Eq. (III.D5) we get

$$\int_{-\infty}^{\infty} d\phi \frac{qW}{\epsilon} = q(\alpha - v)\mathrm{A}^0/m . \quad \text{(III.D9)}$$

Finally, as $\epsilon \to 0$, the reaction (III.B1) takes place in a narrow domain and hence we may write Eq. (III.B4) for the (unchanged) monomer concentration C as

$$\frac{\partial C}{\partial t} = D\frac{\partial^2 C}{\partial x^2} + N\delta(x - vt) + H , \quad \text{(III.D10)}$$

where, using Eq. (III.D9), we have

$$N = \frac{q(\alpha - \beta)\mathrm{B}^0/n}{m(\mathrm{A}^0/m + \mathrm{B}^0/n)} . \quad \text{(III.D11)}$$

Thus, the two important differences between the electrical and nonelectrical configurations are that the former has time independent interface velocity and rate of monomer production whereas, these quantities decrease as $t^{-1/2}$ for the purely diffusional situation. Clearly this is the basis of the periodicity of banding in the presence of an applied electric field.

4. Wave profile and existence criterion

In general, the calculation of the wave profile and conditions of existence are quite difficult. However in the limit $\epsilon \to 0$ the analysis is greatly simplified. Using arguments as in Secs. III.B and III.C, we find that as $\epsilon \to 0$ we have

$$A(\phi)=\begin{cases}0, & \phi>0\\ A_0[1-e^{a\phi}], & \phi<0\end{cases}, \qquad \text{(III. D12)}$$

$$B(\phi)=\begin{cases}B_0[1-e^{b\phi}], & \phi>0,\\ 0, & \phi<0,\end{cases}$$

$$a=(\alpha-v)/D_A, \quad b=(\beta-v)/D_B. \qquad \text{(III. D13)}$$

In order that these solutions satisfy the asymptotic behavior $A\to A_0$ as $\phi\to-\infty$, $B\to B_0$ as $\phi\to+\infty$ we have the conditions

$$\alpha>v, \qquad \text{(III. D14)}$$

$$\beta<v, \qquad \text{(III. D15)}$$

Using Eq. (III. D8) for v these existence criteria imply

$$\alpha>\beta. \qquad \text{(III. D16)}$$

From Eq. (III. D3) this yields

$$z_A M_A E> z_B M_B E. \qquad \text{(III. D17)}$$

This implies that waves can propagate under a variety of conditions. Since we are only interested in cases wherein propagation goes into the tube from the A source $v>0$, we limit our discussion to the cases [see Eqs. (III. D3) and (III. D8)] for which

$$\left(\frac{z_A M_A A_0}{m}+\frac{z_B M_B B_0}{n}\right)E>0. \qquad \text{(III. D18)}$$

Thus electroinfusion wave experiments can be carried out when Eqs. (III. D17) and (III. D18) are both satisfied. If Eq. (III. D17) is violated waves do not exist and if Eq. (III. D18) is violated, they propagate in the experimentally uninteresting direction (if they exist). The signs of z_A, z_B, and E are clearly important in these criteria. Also, the concentrations A^0, B^0 and the stoichiometric coefficients m and n may affect the wave propagation direction. Hence, A^0 and B^0 are sometimes useful experimental parameters for changing wave velocity.

Finally, we note that the existence criterion $\alpha>\beta$ implies via Eq. (III. D12) that over the range of wave existence the rate of monomer production, the N factor, is positive, as it should be.

IV. REGULAR BAND INDUCTION IN AN INITIALLY UNIFORM SOL

A. The model

It has long been known that diffusion of one coprecipitate (A) into a region with a uniform sol with its coprecipitate (B) can induce banding in the sol. Here we simulate this situation with the competitive particle growth model. With Eqs. (II. B9) and (II. B10) we have the equations

$$\frac{1}{\beta}\frac{\partial\sigma}{\partial\tau}=\frac{\partial^2\sigma}{\partial\xi^2}+\mu(t)\delta[\xi-S(t)]-\Psi^2\nu\frac{\partial\Psi}{\partial\tau}, \qquad \text{(IV. A1)}$$

$$\frac{\partial\Psi}{\partial\tau}=\sigma-g(\Psi), \qquad \text{(IV. A2)}$$

$$\mu(\tau)=\bar{R}\bar{t}N(\bar{t}\tau)/C^{eq}(\infty)L\Gamma, \quad S(\tau)=X(\bar{t}_\tau)/L, \qquad \text{(IV. A3)}$$

where $N(t)$ and $X(t)$ are given by Eqs. (III. C6), and (III. B20), (III. B22), (III. B23) for the electric field free system and by Eq. (III. D11) and $X(t)=vt$ with v as in Eq. (III. D8) for the electrical problem. In Eqs. (IV. A1) and (IV. A2), ξ is the dimensionless spatial variable and not the similarity variable defined in Sec. III. All other variables are defined in Sec. III B.

For a tube of length $L_T\gg L$, the A infusion experiment corresponds to the following initial data:

$$\Psi(\xi,0)=\Psi_>, \quad \sigma(\xi,0)=g(\Psi_>). \qquad \text{(IV. A4)}$$

For simplicity we assume that the monomer does not escape from the end of the tube into which A is being introduced; hence we take the no flux boundary condition

$$D\partial\sigma/\partial\xi=0, \quad \text{at } \xi=0. \qquad \text{(IV. A5)}$$

This approximates the situation where the A reservoir is small in volume (but highly concentrated in A so that A is approximately constant during experiment). If the A reservoir is large in volume and stirred, then the boundary condition $\sigma(0,\tau)=-\bar{R}/\Gamma$ may be more accurate although the resulting "end effects," leading to dissolution of precipitate near $\xi=0$, will not be considered further here.

B. Electroinfusion waves

Under the influence of the electrically driven A infusion, monomer is produced at a constant rate at a position which moves at constant velocity as discussed in Sec. III D. This moving source will tend to increase the average particle size in its wake as it encroaches into the uniform sol. In this section, we investigate the possiblity that a constant velocity and profile of coarsening—an "electroinfusion coarsening wave"—exists. In the next section, we examine this problem numerically and determine when this solution becomes unstable and leads to undulatory precipitation phenomena.

1. *The wave equations*

We seek solutions that keep in step with the monomer source. The latter travels at a speed v given in Sec. III D. Introducing a dimensionless speed $u=\bar{t}v/L$, the wave profile $\sigma=\sigma(\eta)$, $\Psi=\Psi(\eta)$ and $\eta=\xi-u\tau$, Eqs. (IV. A1) and (IV. A2) become

$$\sigma''+\frac{u}{\beta}\sigma'+\tfrac{1}{3}u(\Psi^3)'+\mu\delta(\eta)=0, \qquad \text{(IV. B1)}$$

$$u\Psi'+\sigma-g(\Psi)=0, \qquad \text{(IV. B2)}$$

where "$'$" denotes a derivative with respect to η.

2. *Constants of wave motion*

From Eq. (IV. B1) it is evident that for $\eta\neq0$, there is a constant of the motion. Thus, we have

$$\sigma'+\frac{u\sigma}{\beta}+\tfrac{1}{3}u\Psi^3=Q_{\lessgtr}, \quad \eta\gtrless0. \qquad \text{(IV. B3)}$$

The constants $Q_{\gtrless}$ can be evaluated under the assumption that the wave corresponds to a uniform sol of particles of radius $\Psi_{\gtrless}$ for $\eta\to\pm\infty$, respectively. Thus,

$$Q_{\gtrless} = \frac{u}{\beta} g(\Psi_{\gtrless}) + \tfrac{1}{3} u \Psi_{\gtrless}^3 . \qquad \text{(IV.B4)}$$

The constants $Q_{\gtrless}$ can be related by integrating Eq. (IV.B1) over a small interval $(0^-, 0^+)$ around $\eta = 0$. Since σ is continuous at $\eta = 0$, this integration yields

$$\sigma'(0^+) - \sigma'(0^-) - u[\Psi^3(0^+) - \Psi^3(0^-)] + \mu = 0 . \qquad \text{(IV.B5)}$$

Using Eq. (IV.B5) we thus find

$$Q_< = Q_> + \mu . \qquad \text{(IV.B6)}$$

Thus, Eq. (IV.B4) and (IV.B6) show that $\Psi_>$ and $\Psi_<$ are connected by a total mass conservation law

$$\frac{1}{\beta} g(\Psi_<) + \tfrac{1}{3} \Psi_<^3 = \frac{1}{\beta} g(\Psi_>) + \tfrac{1}{3} \Psi_>^3 + \mu , \qquad \text{(IV.B7)}$$

stating that the amount of substance in both particles and solution after arrival of the source is that far in advance of the source plus that added by it.

3. A closed equation for Ψ

We next express the problem in the form of a closed set of equations in Ψ by eliminating σ from the profile equations. Solving Eq. (IV.B2) for σ and inserting the result in Eq. (IV.B3) we get

$$[g(\Psi) - u\Psi']' + \frac{u}{\beta}[g(\Psi) - u\Psi'] + \tfrac{1}{3} u \Psi^3 = Q . \qquad \text{(IV.B8)}$$

To completely solve this problem we must obtain two conditions relating Ψ and Ψ' across the source at $\eta = 0$. We also have the asymptotic data

$$\Psi \underset{\eta \to \pm\infty}{\sim} \Psi_{\gtrless} . \qquad \text{(IV.B9)}$$

Integration of Eq. (IV.B2) over the interval $[0^-, 0^+]$ we get the continuity condition for Ψ,

$$\Psi(0^+) = \Psi(0^-) . \qquad \text{(IV.B10)}$$

The remaining condition needed to completely specify the solution comes from the fact that continuity of σ and Ψ at $\eta = 0$ implies, through Eq. (III.B2), that Ψ' is also continuous at $\eta = 0$; thus,

$$\Psi'(0^+) = \Psi'(0^-) . \qquad \text{(IV.B11)}$$

4. Small amplitude waves

If the source strength μ is small, then so is $\Psi_< - \Psi_>$ and hence the coarsening wave can be viewed as a small deviation from uniformity. We now seek a small μ description of the waves. First, introduce a deviation function ϕ such that

$$\Psi = \Psi_{\gtrless} + \phi, \quad \text{in } \eta \gtrless 0. \qquad \text{(IV.B12)}$$

Inserting these definitions in Eq. (IV.B8) and neglecting nonlinear terms in ϕ we obtain, letting $f = dg/d\Psi$,

$$-u\phi'' + [f_{\gtrless} - u^2/\beta]\phi' + u[f_{\gtrless}/\beta + \Psi_{\gtrless}^2]\phi = 0 . \qquad \text{(IV.B13)}$$

This equation yields solutions of the form $\phi = Ae^{\omega\eta}$ with ω satisfying

$$-u\omega^2 + [f_{\gtrless} - u^2/\beta]\omega + u[f_{\gtrless}/\beta + \Psi_{\gtrless}^2] = 0 . \qquad \text{(IV.B14)}$$

The two roots of Eq. (IV.B14) denoted $\omega_\pm$ are given by

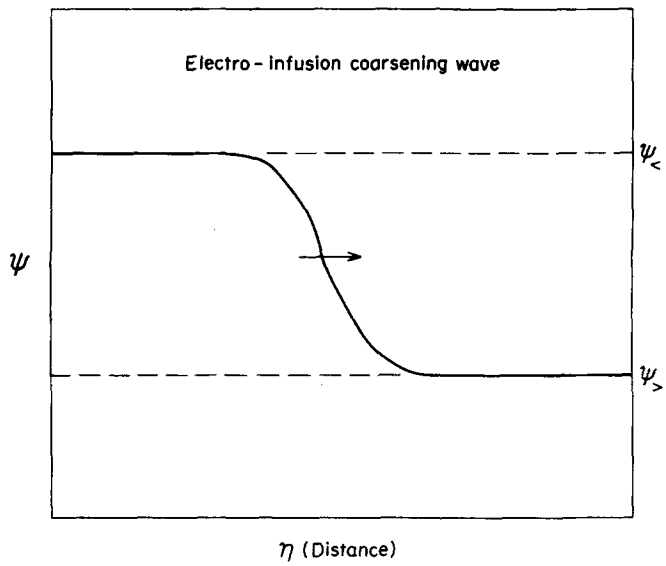

FIG. 16. Idealized coarsening wave driven by electroinfusion monomer source. In numerical simulations it was found to be unstable but serves a most important theoretical role as an organizing tool for unraveling complex pattern forming phenomena.

$$\omega_\pm = \tfrac{1}{2} u [f_{\gtrless} - u^2/\beta] \pm \frac{1}{2} \sqrt{\frac{1}{u^2}[f_{\gtrless} - u^2/\beta]^2 + 4[f_{\gtrless}/\beta + \Psi_{\gtrless}^2]} . \qquad \text{(IV.B15)}$$

The present theory is valid as $\mu \to 0$ and hence $f_>$ and $f_<[\equiv f(\Psi_{\gtrless})]$ are approximately equal. But since $\phi = Ae^{\omega\eta}$ and $\phi \to 0$ as $\eta \to \pm\infty$, we must have the real part of one $\omega < 0$ for $\eta > 0$ and one $\omega > 0$ for $\eta < 0$. This holds if and only if $f/\beta + 3\Psi^2 > 0$ for $\Psi = \bar{\Psi} \equiv \frac{1}{2}[\Psi_> + \Psi_<]$. Clearly, $\omega_\pm \gtrless 0$ in this case. Hence, we have

$$\Psi = \begin{cases} \Psi_> + A_> e^{\omega_- \eta}, & \eta > 0 \\ \Psi_< + A_< e^{\omega_+ \eta}, & \eta < 0 . \end{cases} \qquad \text{(IV.B16)}$$

Continuity of Ψ and Ψ' at $\eta = 0$ demands

$$\Psi_> + A_> = \Psi_< + A_< ,$$

$$\omega_+ A_< = \omega_- A_> . \qquad \text{(IV.B17)}$$

Solving these equations for $A_{\gtrless}$ and using Eqs. (IV.B4) and (IV.B6) considering $\Psi_{\gtrless} - \Psi$ to be small, we obtain

$$\Psi = \begin{cases} \Psi_> + \dfrac{\omega_+}{\omega_-} A e^{\omega_- \eta}, & \eta > 0 , \\ \Psi_< + A e^{\omega_+ \eta}, & \eta < 0 . \end{cases} \qquad \text{(IV.B18)}$$

$$A = \frac{\beta \mu \omega_-}{u[f + \beta\bar{\Psi}^2][\omega_+ - \omega_-]} . \qquad \text{(IV.B19)}$$

From Eq. (IV.B14), we see that $\omega_+ \omega_- > 0$. Hence, $A < 0$ as it should be. This profile is shown in Fig. 16. Having established the existence of monotonic propagating profiles of particle coarsening induced by electroinfusion, we next turn to the question of their stability and the occurrence of undulatory phenomena.

C. Simulation of electroinfusion waves and cross flux banding

Far in advance and behind the transition region of the waves studied above, the system is a uniform sol. As we have discussed this uniform sol is typically unstable to pattern formation. Hence, it is clear that the electroinfusion coarsening waves are never strictly stable. Nonetheless, the concept of a coarsening waves serves as a useful starting point for the understanding of a host of complex phenomena that can arise when the experimental situation shown in Fig. 15 is used.

1. Coarsening waves and banding in a pre-existing sol

A series of simulations of the electrocross infusion of coprecipitates in a pre-existing sol was undertaken using the model Eqs. (IV.A1) and (IV.A2). The δ function was replaced by a unit normalized Gaussian of half-width on the order of the space grid spacing.

A well developed coarsening wave arises for the parameter choice used in Fig. 17. The profile is essentially a monotonically decreasing transition layer of particle size as predicted in the previous section. Notice the small minimum at the left-hand end however. This effect arises because the layer adjacent to the left-hand boundary receives monomer only from the center and left wing of the source of moving monomer production, whereas all regions to the right receive monomer from both wings and the center of the source. Thus,

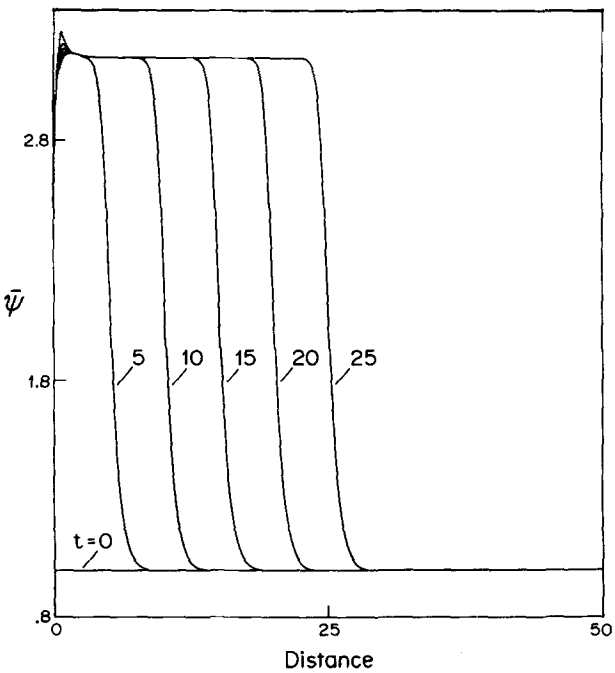

FIG. 17. Simulation of an electroinfusion coarsening wave obtained by numerical solution of Eqs. (IV.A1) and (IV.A2) as described in Sec. IV C. In this experiment an apparatus as shown in Fig. 15 is used to induce a constant velocity interface of monomer production. Note that the coarsening wave satisfies the conservation law (IV.37). At the left boundary the wave is breaking up due to the initial conditions that are amplified by the inherent homogeneous sol instability. Parameters used are $\beta=10$, $u=1$, $\mu=10$, $\Psi_c=0.2$.

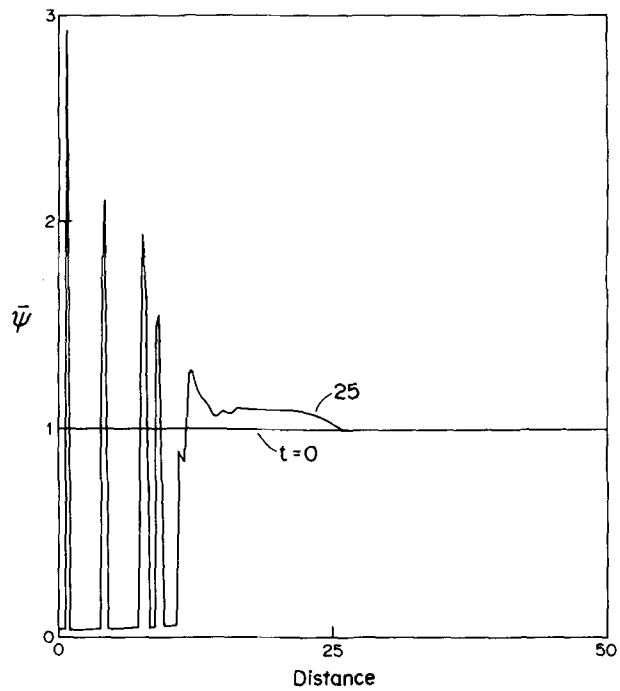

FIG. 18. Same as Fig. 17, except that the monomer source strength $\mu=0.1$. Note that this wave is unstable and rapidly evolves into banding in its wake.

the region just to the right of the left boundary layer has a competitive advantage over the particle size minimum region at the left boundary. We might therefore expect band induction to take place in the wake of the coarsening soliton starting from this end effect. This is seen clearly in Fig. 18 where the banding develops quite quickly for the same β and u but weaker source strength μ. This is because at high source strength the particles in the wake of the front are large and hence the pattern inducing feedback is weak. Finally, note that in both cases shown (Figs. 17 and 18) the wave conservation law [Eq. (IV.B7)] is obeyed.

These phenomena of Figs. 17 and 18 are quite transparent since coarsening wave propagation and pattern formation are well separated events. A stronger interaction of pattern formation and wave propagation takes place when the wave advancement velocity u becomes on the order of the velocity of pattern advancement, i.e., ξ_1 divided by a typical time for induction of a first satellite, denoted $\tau_1(\beta)$. Thus, the transition velocity u_c is expected to roughly be given by

$$u_c(\beta) \approx \frac{\xi_1}{\tau_1(\beta)}. \qquad \text{(IV.C1)}$$

Since τ_1 decreases with β, $u_c(\beta)$ increases with β. In Figs. 19 and 20 we show simulations that verify these predictions.

D. Simulation of cross diffusion pattern induction in uniform sols

The uniform sol also tends to become patterned when a monomer source, due to interdiffusion as discussed in

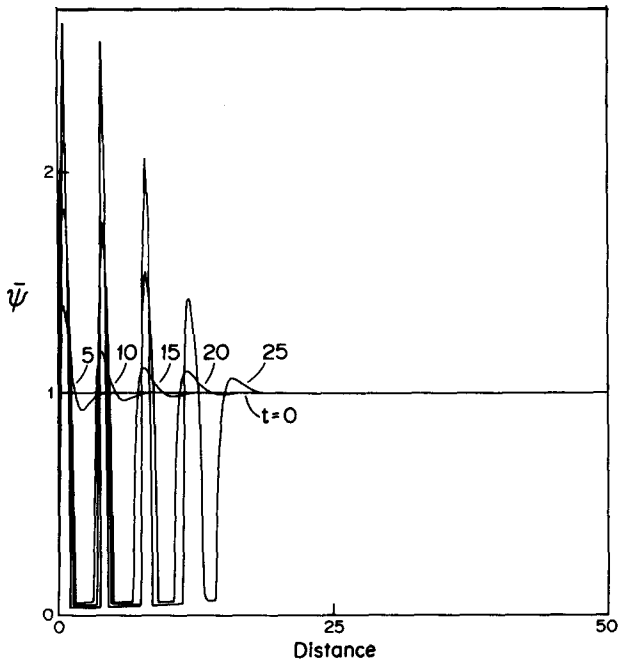

FIG. 19. Same as Fig. 18, except that the advancement rate $u=0.3$. At these conditions the pattern advancement rate exceeds the velocity of front propagation and the front is not observed.

Sec. III A. 3, encroaches into the sol. Here we present numerical simulations of some of the resulting complex phenomena.

1. The model

Our description of these phenomena shall be via Eqs. (IV. A1) and (IV. A2). For the diffusion experiment this becomes

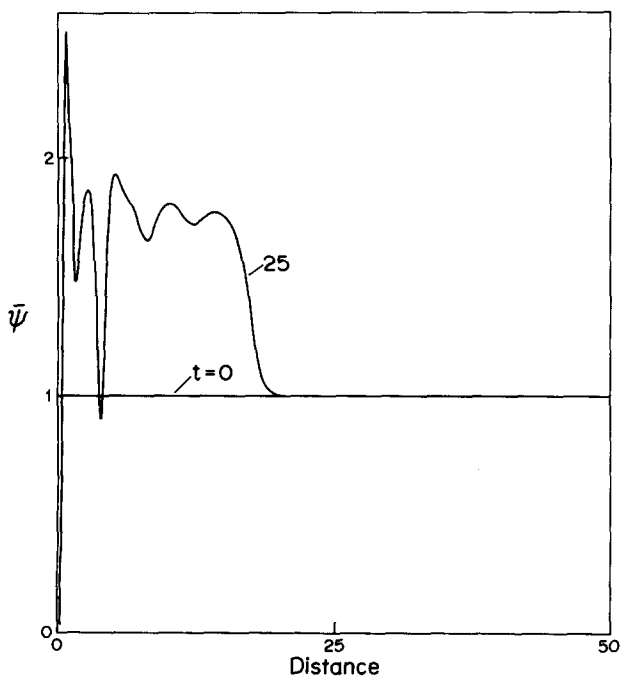

FIG. 20. Same as Fig. 18, except $\mu=7$. Note that the front is clearly present except that it has an interesting scalloped structure.

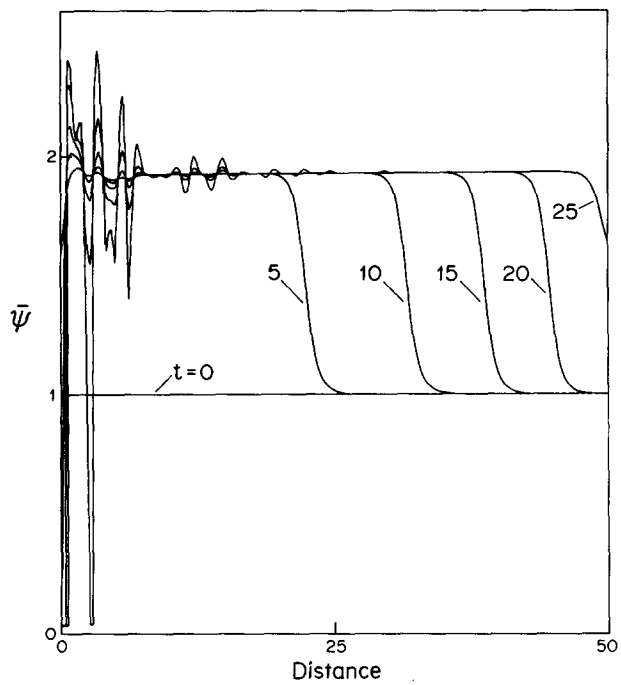

FIG. 21. Simulation of cross-diffusion experiment into a preexisting, initially uniform sol at $\beta=10$, $\Psi_c=0.2$. The source strength parameter λ is 10 and the advancement rate γ is 10 [see Eqs. (IV. D)–(IV. D3) for definitions]. We observe a slowing wavelike intrusion with pattern formation in its wake.

$$\frac{1}{\beta}\frac{\partial\sigma}{\partial\tau}=\frac{\partial^2\sigma}{\partial\xi^2}+\frac{\lambda}{\tau^{1/2}}\delta(\xi-\gamma\tau^{1/2})-\Psi^2\frac{\partial\Psi}{\partial\tau}\ , \qquad \text{(IV. D1)}$$

$$\frac{\partial\Psi}{\partial\tau}=\sigma-g(\Psi)\ , \qquad \text{(IV. D2)}$$

$$\gamma=\alpha\bar{l}^{1/2}L,\quad \lambda=\bar{R}\Lambda/C^{eq}(\infty)L\Gamma\bar{l}^{1/2}\ , \qquad \text{(IV. D3)}$$

where α and Λ are defined in Eqs. (III. B22), (III. B23), and (III. C6), respectively.

2. Diffusive coarsening fronts and their transitions to patterning

In the simulation of Fig. 21 we see a coarsening front which advances with essentially constant profile but, unlike for the electroinfusion coarsening wave, with decreasing velocity. The transition zone is localized to the source at $\gamma\tau^{1/2}$. The constancy of the diffusion front is at first surprising but can be understood in light of the fact that the rate of monomer production decreases as $\tau^{-1/2}$ and hence the amount of monomer produced per unit length is constant. However, the dip at the left-hand end of the tube induced by the initial infusion tends to pattern the wake of the diffusion front. This effect is greatly enhanced by lowering λ, the monomer production rate constant. In Fig. 22 we see the result of a simulation identical to that of Fig. 21 except with a lower value of λ. Notice that because of the greater instability at smaller particle size, the banding keeps up with the front propagation. Note also that the envelope of local particle radius maxima takes on a complex, nonperiodic, undulatory form.

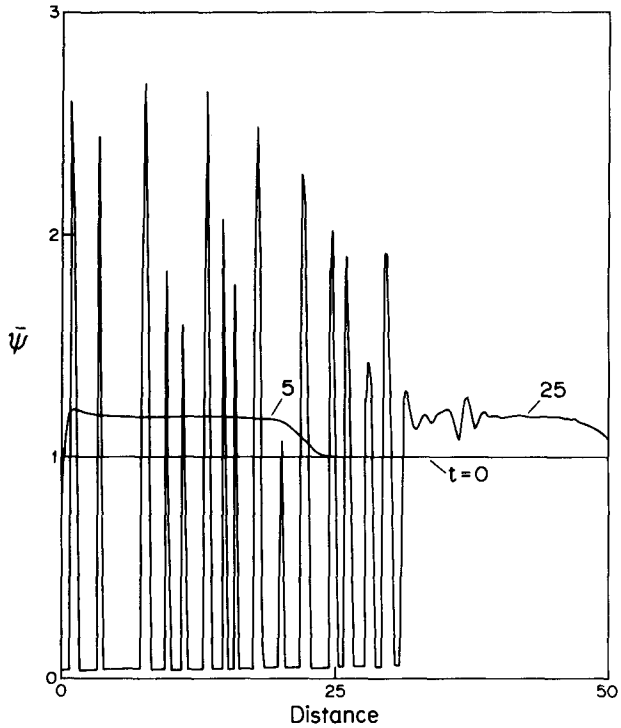

FIG. 22. Same as in Fig. 21, except for smaller source strength $\lambda = 1$. Note the weaker source strength leads to a smaller amplitude and hence much more unstable coarsening wave. The resulting banding has interesting irregular spacing and amplitude.

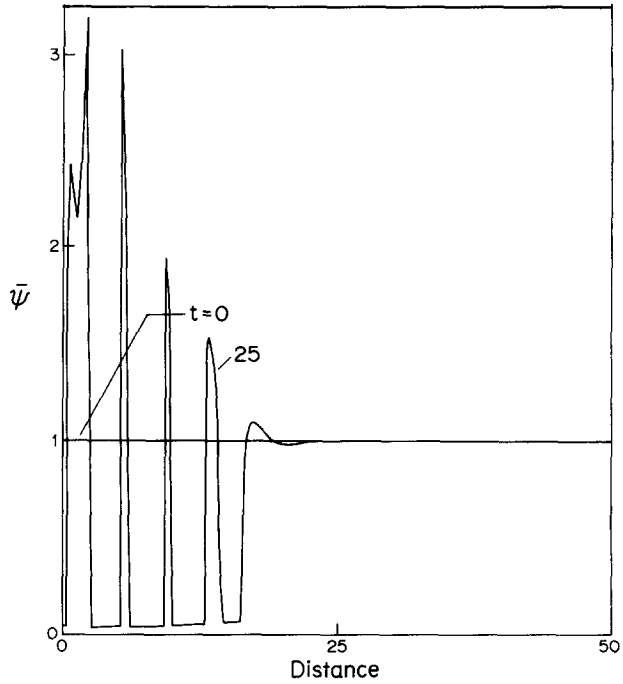

FIG. 24. Same as Fig. 23 with $\gamma = 1$, $\lambda = 1$. At this slow advancement rate a decelerating wave is never created. Patterning is regular. Note the secondary bandinglike splitting of the maximum at the far left near the A source.

At lower advancement constant γ, the pattern encroachment keeps up with the naiscent front so the latter never actually is observed. This repression of the diffusion coarsening front persists even at high monomer production rates as seen in Figs. 23 and 24. In fact the main effect of higher λ is only to amplify the pattern but not to change its spacing.

At intermediate values of γ, the pattern rate is observed to catch up to the initially manifest coarsening front and a cross over effect will be observed as seen in Figs. 25 and 26.

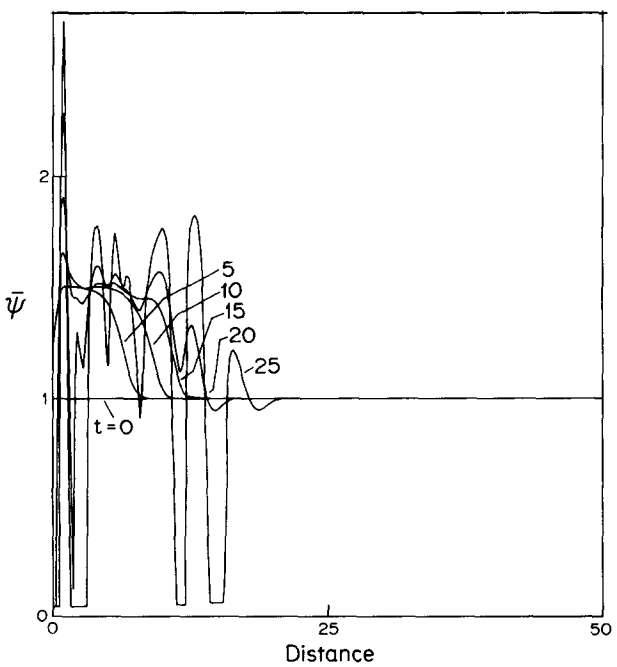

FIG. 23. Same as Fig. 22 except that the advance rate is slower, i.e., $\gamma = 3$. Note that a slowing diffusional wave attempts to propagate but because it slows down, the pattern advancement rate catches up and exceeds it.

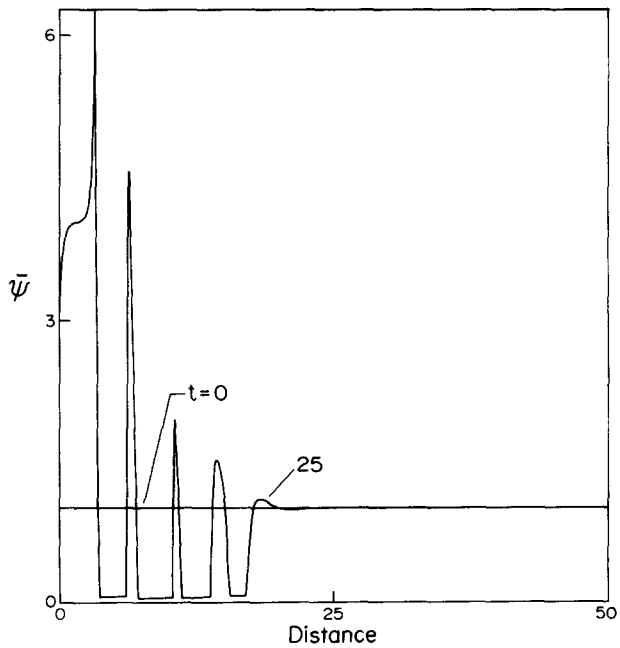

FIG. 25. Same as Fig. 24 except at increased source strength, $\lambda = 10$. The patterns in Figs. 24 and 25 are essentially identical except for amplitude. In particular the pattern spacing appears to be independent of λ for these slow advancement rates ($\gamma = 1$).

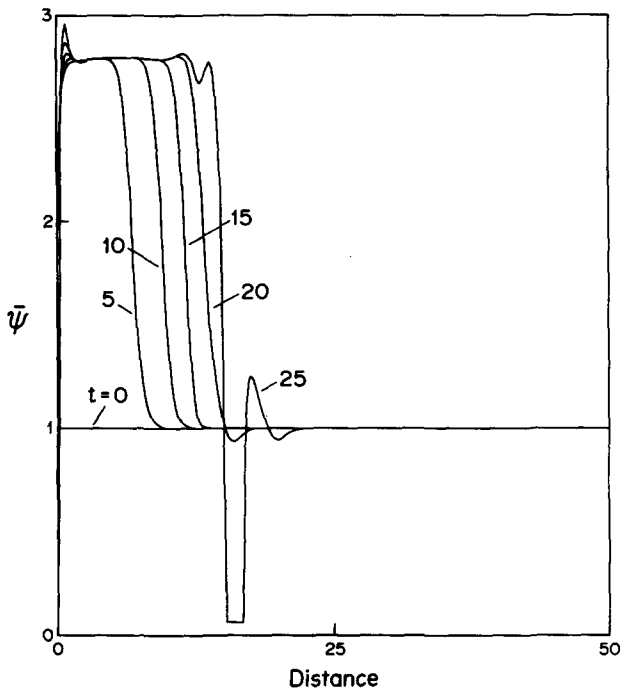

FIG. 26. Same as Fig. 24 with $\gamma=3$, $\lambda=10$. Note the decelerating wave decays into a pattern advancement mode when it becomes slower than the latter.

V. CONCLUSIONS

The competitive particle growth theory of precipitation banding shows the existence of a variety of nonlinear phenomena including spontaneous pattern formation and the propagation and instability of waves. These effects are being directly tested in our laboratory and will be reported elsewhere.[13]

One of the most surprising consequences of the theory is the independence of the first satellite induction length on β. This length is a strictly nonlinear effect as the linear stability analysis of Sec. IIC did not suggest any such characteristic length. It is also noteworthy that this characteristic length is typically much longer than the mean interparticle distance $n^{-1/3}$, where the theory breaks down. Indeed, it was assumed that there were many particles within the typical length scale of interest in our initial formulation of the theory and hence our results show our approach to be self-consistent.

The present model has the following basic mathematical structure. A diffusible substance (monomer) interacts with an immobile variable (particle radius). This turns out to be in close analogy to a variety of other phenomena involving spontaneous pattern formation in systems involving transport and first order phase transitions. Such effects are most striking in geology. In the case of metamorphic layering a polycrystalline multimineralic medium (a rock) becomes banded in mineral content.[3,18] The kinetic processes here are, as in the present system, crystal growth and dissolution. However, the feedback leading to instability is due to the dependence of the equilibrium constant on the local state of stress and hence on the types of crystals surrounding a given crystal. Another example is that of spontaneous stylolite formation. Stylolites are seams that spontaneous appear in limestone and sandstone that were, apparently, subject to anisotropic stress. Again, the feedback that allows for the "nucleation" and growth of seams and the regularity of their spacing is related to the effects of anisotropic stress although here the porosity plays an important role.[19] In both cases—metamorphic layering and stylolitization—the mathematical structure is that a set of nondiffusible variables interacts with diffusible ones. Thus these two examples from geology and a number of others not yet mathematically modeled,[3] appear to constitute a large class of very interesting spontaneous pattern formation phenomena that is sure to receive much attention in the near future.

[1]R. E. Liesegang, Phot. Archiv. 21, 221 (1896).
[2]E. Hedges and J. E. Myers, *The Problem of Physico-Chemical Periodicity* (Longmans-Green, New York, 1926).
[3]P. Ortoleva, J. Chadam, M. El-Badewi, R. Feeney, D. Feinn, S. Haase, R. Larter, E. Merino, A. Strickholm, and S. Schmidt, Mechanisms of Bio- and Geo-Pattern Formation and Chemical Signal Propagation in *Proceedings of a Workshop on Instabilities, Bifurcations and Fluctuations* held in Austin, Texas, March 1980.
[4]K. H. Stern, Natl. Bur. Stand. (U.S.) Spec. Publ. No. 292 (1967).
[5]W. Ostwald, Kolloid-Z. 36, 380 (1925).
[6]S. Prager, J. Chem. Phys. 25, 279 (1956).
[7]M. R. Flicker and J. Ross, J. Chem. Phys. 60, 3458 (1974).
[8]D. Feinn, P. Ortoleva, W. Scalf, S. Schmidt, and M. Wolff, J. Chem. Phys. 67, 27 (1978).
[9]R. Lovett, J. Ross, and P. Ortoleva, J. Chem. Phys. 69, 947 (1978).
[10]T. -M. Ahn and J. K. Tien, J. Chem. Solids 37, 771 (1976).
[11]J. Heicklen, *Colloid Formation and Growth* (Academic, New York, 1976).
[12]D. V. Von Rosenberg, *Methods for the Solution of Partial Differential Equations* (Elsevier, New York, 1969).
[13](a) R. Feeney and P. Ortoleva (in preparation); (b) R. Feeney, P. Strickholm, and P. Ortoleva (in preparation).
[14]E. Heiney and P. Ortoleva (unpublished); these results were briefly reviewed by P. Ortoleva in *Theoretical Chemistry*, edited by H. Eyring (Academic, New York, 1978), Vol. IV.
[15]S. Schmidt and P. Ortoleva, J. Chem. Phys. 72, 2733 (1980).
[16]S. Schmidt and P. Ortoleva, J. Chem. Phys. 74, 4488 (1981).
[17]G. W. Bluman and J. D. Cole, *Similarity Methods for Differential Equations* (Springer, New York, 1974).
[18]P. Ortoleva, E. Merino, and P. Strickholm, Am. J. Sci. (to be published).
[19]P. Strickholm, E. Merino, and P. Ortoleva (submitted).
[20]S. Kai, S. C. Miller, and J. Ross, "Measurements of Temporal and Spatial Sequences of Events in Periodic Precipitation Processes" (preprint).